

1-22-2019

## MODELING OF LEAKAGE THROUGH FAULT-ZONE STRUCTURES IN CO<sub>2</sub> GEOLOGICAL STORAGE

Dayna Rodriguez Zambrano

*Louisiana State University and Agricultural and Mechanical College*

Follow this and additional works at: [https://digitalcommons.lsu.edu/gradschool\\_theses](https://digitalcommons.lsu.edu/gradschool_theses)



Part of the [Environmental Engineering Commons](#), and the [Petroleum Engineering Commons](#)

---

### Recommended Citation

Rodriguez Zambrano, Dayna, "MODELING OF LEAKAGE THROUGH FAULT-ZONE STRUCTURES IN CO<sub>2</sub> GEOLOGICAL STORAGE" (2019). *LSU Master's Theses*. 4842.

[https://digitalcommons.lsu.edu/gradschool\\_theses/4842](https://digitalcommons.lsu.edu/gradschool_theses/4842)

This Thesis is brought to you for free and open access by the Graduate School at LSU Digital Commons. It has been accepted for inclusion in LSU Master's Theses by an authorized graduate school editor of LSU Digital Commons. For more information, please contact [gradetd@lsu.edu](mailto:gradetd@lsu.edu).

# **MODELING OF LEAKAGE THROUGH FAULT-ZONE STRUCTURES IN CO<sub>2</sub> GEOLOGICAL STORAGE**

A Thesis

Submitted to the Graduate Faculty of the  
Louisiana State University and  
Agricultural and Mechanical College  
in partial fulfillment of the  
requirements for the degree of  
Master of Science in Petroleum Engineering

in

The Craft & Hawkins Department of Petroleum Engineering

by

Dayna Rodriguez Zambrano  
B.S., Universidad Mayor de San Andres, 2012  
M.S., Universidad Mayor de San Andres, 2014  
May 2019

© 2019  
Dayna Rodriguez Zambrano  
ALL RIGHTS RESERVED

*To my parents Juan and Yermmy,  
to Flaquillo and Kat,  
and to all dreamers.*

## **Acknowledgements**

There are not enough words that could express my enormous gratitude to Dr. Mehdi Zeidouni for having accepted me as a member of his research team ITARC. I was truly honored to work under his supervision and I thank him for all the hours dedicated to my research, for his invaluable guidance, and for his support. Also, thanks for the many times he has demanded more from me and my work. I will surely carry a learning for life.

I would also like to thank Dr. Zulqarnain for his help with the models and the simulation work, and the several meetings with very fruitful analysis. Also, many thanks to Dr. Hannon for all his help, his predisposition and guidance in the meetings, and his detailed revisions and comments of my work. To Dr. Kam as graduate advisor and as part of my committee, his help and advice has been unmeasurably valuable during this last year at LSU.

Thanks to the Fulbright program for having supported one of my life dreams, studying in the United States of America. Thanks for allowing me to experience life in a land of opportunities and diversity. Thanks, because I was inspired constantly by people from all over the world inside and outside the academia. I hope one day I give back to my community and country as much as the Fulbright Program has given me.

This work would not have been possible without the contribution of the Computer Modelling Group LTD that provided a free license of their reservoir simulation software to the department of Petroleum Engineering.

My eternal gratitude to my parents Yermmy Zambrano and Juan Rodriguez, and to my siblings Brian and Kathleen for their unconditional love and support during this journey.

Thanks to Abdullah Al-Tameemi for his persistent positive view of life, for being my personal cheerleader and emotional coach. Also, many thanks to Dr. Watheq Al-Mudhafar for having trusted in me and helped me when I needed it the most.

To my dear friends for life Gabriela Mayta, Mery Flores, Gerardo Sangüeza, and Flor Yabar thank you for your friendship and for the very long conversations listening to my adventures, complains, frustrations, and most importantly for always believing in me.

Finally, thanks to all the friends that I encountered at LSU that have given me their support during this time.

## Table of Contents

|  |      |
|--|------|
| Acknowledgements .....   | iv   |
| List of Figures .....  | viii |
| List of Tables .....   | xi   |
| Abstract.....  | xii  |
| Chapter 1. Introduction .....  | 1    |
| 1.1. Background .....  | 1    |
| 1.2. Problem Statement .....   | 3    |
| 1.3. Anticipated Results .....   | 4    |
| 1.4. Research Objectives.....  | 5    |
| Chapter 2. CO <sub>2</sub> Trapping Mechanisms in Deep Saline Aquifers.....  | 6    |
| 2.1. Structural/stratigraphic Trapping .....   | 6    |
| 2.2. Residual Trapping .....   | 7    |
| 2.3. Solubility Trapping .....   | 7    |
| 2.4. Mineral Trapping .....  | 8    |
| Chapter 3. Fault Structure and Effects on CO <sub>2</sub> Sequestration .....                                      | 9    |
| 3.1. Fault Permeability .....  | 11   |
| 3.2. CO <sub>2</sub> Leakage through Faults .....  | 12   |
| Chapter 4. Multiphase Fluid Flow coupled with Geomechanics for CO <sub>2</sub> storage in Saline<br>Aquifers ..... | 14   |
| 4.1. Barton-Bandis Model for Fracture Permeability .....   | 16   |
| 4.2. Fault Influence on CO <sub>2</sub> geological storage .....   | 18   |
| Chapter 5. Model Validation: Fluid Flow Simulation Coupled with Geomechanics .....                                 | 20   |
| Chapter 6. Simulation of a Representative Model with an Idealized Sealing Fault .....                              | 25   |
| 6.1. Model Description .....   | 25   |
| 6.2. Results .....   | 28   |
| Chapter 7. Coupled Modeling of a Geologically Realistic Fault Effect on CO <sub>2</sub> Storage<br>Integrity ..... | 40   |
| 7.1. Model Description .....   | 40   |
| 7.2. Simulation results .....  | 43   |

|                              |    |
|------------------------------|----|
| Chapter 8. Conclusions ..... | 54 |
| References... ..             | 56 |
| Vita.....                    | 59 |



## List of Figures

|  |    |
|--|----|
| Figure 1.1. Options for CO <sub>2</sub> geological sequestration .....   | 2  |
| Figure 1.2. Schematic of a fault structure and fractures in its damage zone.. ....   | 4  |
| Figure 2.1. A schematic representation of three trapping mechanisms of CO <sub>2</sub> in saline<br>aquifers .....   | 6  |
| Figure 3.1. Generic classification of faults: normal, reverse and strike-slip faults. ....   | 9  |
| Figure 3.2. Simplified scheme of a typical fault structure, where there are a fractured<br>damage zone and a high-strain core .....  | 10 |
| Figure 3.3. Possible paths of CO <sub>2</sub> migration due to the formation of fracture networks as a<br>result of injection pressure in a naturally fractured caprock. ....  | 13 |
| Figure 4.1. Flowchart for iterative coupling of fluid flow simulation with geomechanics .....  | 16 |
| Figure 4.2. Fracture permeability based on modified Barton-Bandis model.....   | 17 |
| Figure 5.1. Gas and water relative permeability curves used in the validation model .....  | 22 |
| Figure 5.2. Reservoir description for the validation model: horizontal and vertical<br>permeability in the aquifer, caprocks, overburden-1, and overburden-2 .....   | 22 |
| Figure 5.3. Normal fracture effective stress at center of Caprock 2 and the center of the base<br>of the Overburden 2.....   | 23 |
| Figure 5.4. Vertical displacement of Caprock 2. Vertical displacement increases gradually<br>during CO <sub>2</sub> injection.....   | 23 |
| Figure 5.6. A) Contour map of CO <sub>2</sub> gas saturation distribution after four years of injection<br>presented by (Tran et al., 2009). B) Contour map of CO <sub>2</sub> gas saturation<br>distribution after four years of injection obtained by the validation model. .... | 24 |
| Figure 6.1. Cross-sectional configuration of the simple geometry model. ....   | 26 |
| Figure 6.2. Gas and water relative permeability curves in the Mt. Simon sandstone in<br>Western Ohio used for the simple geometry model .....  | 27 |
| Figure 6.3. CO <sub>2</sub> mole fraction in the matrix for the dual-permeability fault model with<br>simple geometry .....  | 30 |
| Figure 6.4. CO <sub>2</sub> mole fraction in the fractures of the damage zone for the dual-permeability<br>fault model with simple geometry. ....  | 31 |

|   |    |
|---|----|
| Figure 6.5. Minimum horizontal stress in the matrix for the dual-permeability fault model with simple geometry .....  | 32 |
| Figure 6.6. Vertical fracture permeability changes due to Geomechanics .....  | 33 |
| Figure 6.7. Porosity changes due to Geomechanics– Matrix. Contour graphs of the damage zone for the dual-permeability fault model with simple geometry. ....  | 34 |
| Figure 6.8. Location of the seven blocks used to study permeability, pressure and normal effective stresses during ten years of CO <sub>2</sub> injection. ....   | 36 |
| Figure 6.9. Normal effective stresses and permeability changes for blocks 4 and 7 throughout the injection period .....   | 37 |
| Figure 6.10. Figures A to D represent minimum horizontal stress changes for locations 1, 2, 3, 4, 5 and 6. ....   | 39 |
| Figure 7.1. Cross-sectional configuration used for the realistic simulation. The model resembles a CO <sub>2</sub> storage site in Louisiana .....  | 41 |
| Figure 7.2. Contour maps of CO <sub>2</sub> mole fraction distribution in the matrix for the dual-permeability model with real geometry at different times during the injection period (after 10, 20 and 30 years) and post-injection (after 40 years of simulation)..... | 44 |
| Figure 7.3. CO <sub>2</sub> mole fraction in the fractures of the damage zone for the model with realistic geometry at different times during the injection period (after 10, 20 and 30 years) and post-injection (after 40 years of simulation).....                     | 45 |
| Figure 7.4. Minimum horizontal stress contour graphs for the realistic model at different times during the injection period (after 10, 20 and 30 years) and post-injection (on 2059 and after 40 years of simulation).....  | 46 |
| Figure 7.5. Evolution of vertical fracture permeability in the damage zone at different times of CO <sub>2</sub> injection and after ten years of injection ceases.....   | 47 |
| Figure 7.6. Location of the 7 blocks used for the analysis of permeability, pressure and minimum effective stress.....  | 48 |
| Figure 7.7. Minimum horizontal stress and pore pressure profiles for locations 3 and 4, both located in the lower sand. The profiles show results for the 30 first years of injection and ten more years of post-injection. ....  | 50 |
| Figure 7.8. Minimum horizontal stress and pore pressure profiles for blocks 1 and 2, both located in the lower sand. The profiles show results for the 30 first years of injection and ten more years of post-injection. ....   | 51 |

|   |    |
|---|----|
| Figure 7.9. Minimum horizontal stress and pore pressure profiles in the middle of the caprock (location 5). The profiles show results for the 30 first years of injection and ten more years of post-injection. ....                          | 52 |
| Figure 7.10. Minimum horizontal stress and pore pressure profiles for location 6 (in the caprock and contiguous to the damage zone). The profiles show results for the 30 first years of injection and ten more years of post-injection. .... | 53 |

## List of Tables

|            |   |    |
|------------|---|----|
| Table 5.1. | Parameters of the injection well used for the validation of the investigation performed by Tran et al. (2009). .....                      | 21 |
| Table 5.2. | Geomechanical rock properties used in the validation model.....   | 21 |
| Table 6.1. | Mechanical properties for the sandstones and the caprock in the simple geometry model .....   | 27 |
| Table 6.2. | Barton-Bandis model parameters applied only for fracture permeability calculations in the damage zones of the simple geometry model ..... | 27 |
| Table 7.1. | Mechanical properties used for the simulation and study of a realistic model .....  | 40 |
| Table 7.2. | Permeability table for the matrix and fractures for the system in the realistic simulation model .....                                    | 42 |
| Table 7.3. | Variables used for calculation of permeability after fractures activation with the Barton-Bandis model in the realistic model setup.....  | 43 |

## **Abstract**

Faults intersecting target geological CO<sub>2</sub> storage zones have important implications for storage integrity. Potential leakage pathways due to fluid over-pressurization are investigated in this project to ensure long-term containment of injected CO<sub>2</sub>. Numerical flow simulations coupled with a geomechanical module are presented in this work with the purpose of determining the extent of CO<sub>2</sub> up-fault migration, the driving mechanisms of leakage and the corresponding response of quantified pore pressure and stress variations.

This study uses dual-continuum models performed by using CMG (2017) to correctly account of flow through fractures in a fault damage zone. Numerical simulations were performed in three steps by gradually adding layers of complexity while ensuring the correctness of simulation results. As the first step, we verify our results by reproducing results published in the literature. In the second step, a simple geometry model including a vertical fault which is laterally sealing was simulated. The last model includes a fault resembling a real feature in a potential CO<sub>2</sub> storage site in north Louisiana. Results for the three cases of study, where the initially dormant fractures of the damage zone become conductive with the inclusion of geomechanics, show migration of CO<sub>2</sub> through the opened cracks into the overlying formations. Also, effective stresses along the damage zone show a generalized reduction with higher fracture permeabilities and increments in pore pressure.

## **Chapter 1. Introduction**

### **1.1. Background**

Greenhouse Gas (CMG) emissions are acknowledged to be the leading cause of global warming and climate change. Carbon dioxide (CO<sub>2</sub>) is the most abundant of these gases in the atmosphere and is responsible for 64% of the greenhouse effect according to the United Nations Framework Convention on Climate Change (Williams, 2002). 85% of CO<sub>2</sub> emissions are produced by the burning of fossil fuels, and they are expected to increase by 130% by 2050 (IEA, 2006). Carbon capture and storage (CCS) is considered an option to mitigate CO<sub>2</sub> emissions from large-scale fossil fuel usage. It offers a short-term solution to mitigate climate change while transitioning towards more efficient, sustainable, and/or low-carbon energy systems in the medium or long term. CCS technologies show potential to reduce CO<sub>2</sub> emissions by 54% in the European Union and 33% globally by 2050 (Stangeland, 2007).

The options for CO<sub>2</sub> geological storage include injection in active and depleted oil and gas reservoirs, deep saline aquifers, and coal seams (Figure 1.1). Saline aquifers provide the most significant storage capacity for sequestered CO<sub>2</sub> and the closest proximity to large point sources of emission such as fossil-fuel power plants (NETL, 2015). Early engineering knowledge of CO<sub>2</sub> sequestration in deep saline aquifers was based on the vast experience of injecting CO<sub>2</sub> for enhanced oil recovery (EOR). However, the importance of the long-term fate of the sequestered CO<sub>2</sub> in saline aquifers typically exceeds that of the typical EOR scenario. In addition, simultaneous fluid extraction and injection in the subsurface in CO<sub>2</sub> EOR leads to minimal pressure perturbations. However, due to the absence of fluid extraction in most CO<sub>2</sub> storage applications, significant overpressure may be experienced that has important implications for CO<sub>2</sub>-storage integrity. Numerous CO<sub>2</sub> storage projects have been deployed and significant research has been

conducted over the past two decades to address knowledge gaps associated with CO<sub>2</sub> storage. Proper modeling at various scales is required which includes a variety of coupled physical, chemical, and mechanical processes namely:

1. Multiphase fluid flow
2. Fluid pressurization and changes in effective stress leading to caprock failure and opening of CO<sub>2</sub> leakage pathways.
3. Mutual dissolution of CO<sub>2</sub> and the in-situ brine.
4. Porosity and permeability alterations due to chemical reactions between fluids and formation minerals.

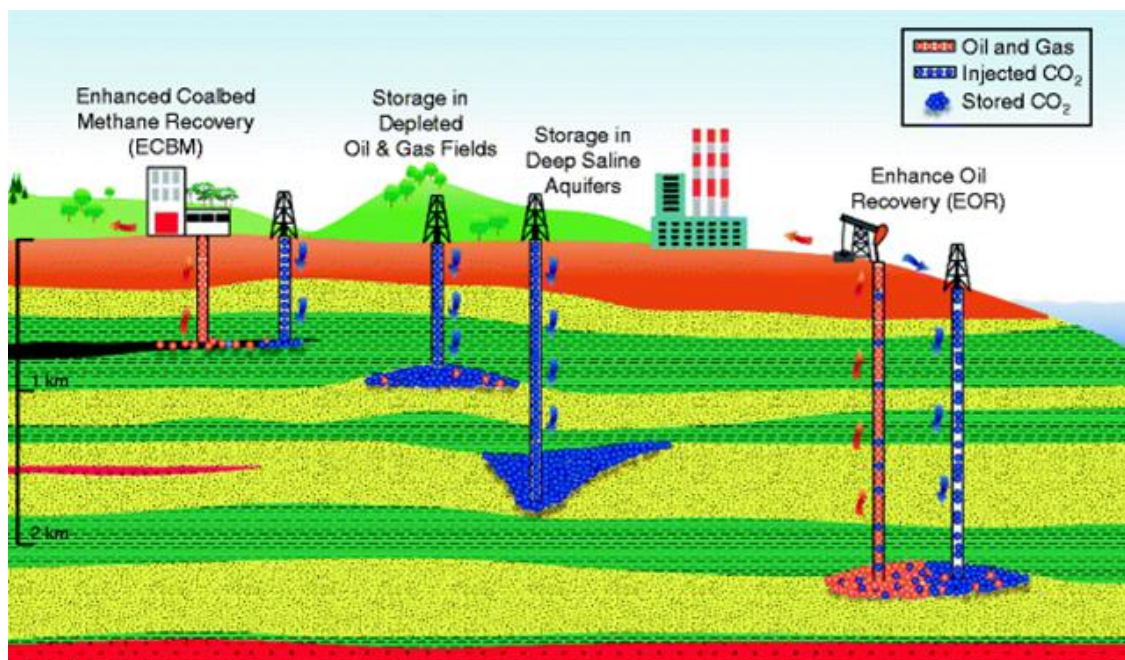


Figure 1.1. Options for CO<sub>2</sub> geological sequestration (Ketzer et al., 2012).

This work focuses on numerical simulations to determine the effects of fault structure on seal integrity for CO<sub>2</sub> sequestration in saline aquifers. Numerical modeling and simulations of these long-term processes are necessary for two reasons. First, it is helpful to understand and evaluate the parameters and processes related to successful CO<sub>2</sub> storage in the presence of faults, which are

abundant in the subsurface. Second, the porosity and permeability alterations occur at rates and scales that may not be captured by laboratory measurements.

## 1.2. Problem Statement

Successful implementation of CO<sub>2</sub> geological storage requires retaining carbon dioxide for at least 1000 years with a leakage rate of less than 0.1% per year (Davidson et al., 2005; Wilson et al., 2007). The success of CO<sub>2</sub>-storage operations depends on many factors. The first is injectivity or dynamic capacity, which relates to the rate and pressure required of CO<sub>2</sub> injection. The second is the static capacity of the aquifer, or how much CO<sub>2</sub> the reservoir can store. The third factor is long-term security, which involves the study of possible CO<sub>2</sub> leakage and which will typically improve with time. These factors are challenges that need to be addressed when studying CO<sub>2</sub> geological sequestration.

In order to ensure effective and successful CO<sub>2</sub> injection, potential leakage pathways of CO<sub>2</sub> must be adequately understood. When CO<sub>2</sub> leaks from the aquifer it could reach buffer aquifers, potable water sources and even the atmosphere (Liu et al., 2010). Evaluation of the storage integrity has to be made in order to plan possible CO<sub>2</sub> storage locations and to identify the leakage quantities for contingency plans and remediation.

Natural and hydraulic fractures are the most important factors when assessing the risk of CO<sub>2</sub> leakage (Liu et al., 2010), and natural fractures are common in possible CO<sub>2</sub> storage locations. The present work intends to provide a better understanding of the coupled fluid flow and mechanical processes during and after injection of CO<sub>2</sub> in saline aquifers, focusing on interactions of these phenomena with dormant fractures in fault zones. This objective is to be accomplished by way of numerical simulations that integrate multiphase flow with geomechanical effects using a



finite-difference compositional flow simulator (CMG, 2017). These simulations are performed using a geological model consisting of a reservoir that is compartmentalized by a laterally sealing fault. The faulted structure comprises a very low-permeability fault core surrounded by dormant fractured damage zones (Figure 1.2).

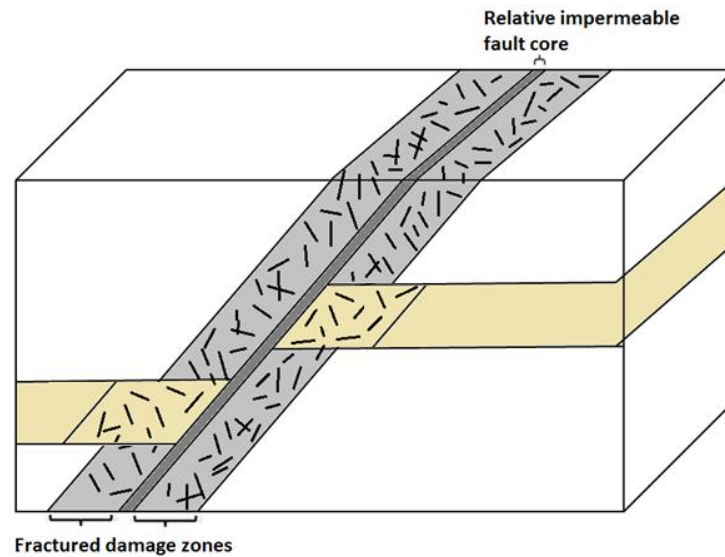


Figure 1.2. Schematic of a fault structure and fractures in its damage zone. High porosity rocks such as sandstones have a thicker damage zone. In this graph, a sandstone is represented by the formation in yellow.

### 1.3. Anticipated Results

Geomechanical processes affect long-term CO<sub>2</sub> geological storage in saline aquifers especially during injection and influence the petrophysical parameters, such as permeability and porosity, of a storage reservoir. In this study, hydro-mechanical modeling is conducted to investigate storage in the presence of a fault zone crosscutting a sequence of sand-shale-sand lithology, as shown in Figure 1.2. This study models natural fractures surrounding a lateral sealing fault with a compositional reservoir simulation iteratively coupled with geomechanics that includes a modified Barton-Bandis model (Bandis et al., 1983) in order to obtain fracture permeabilities (Tran et al., 2009).

Some anticipated results from the numerical simulations are included below.

- The application of geomechanical calculations to the compositional flow model in a compartmentalized aquifer with a lateral fault will result in changes to the transport parameters of the fault structure.
- The mechanically activated dormant fractures in a damaged zone near the CO<sub>2</sub> plume will provide pathways for CO<sub>2</sub> leakage.

#### 1.4. Research Objectives

The objective of this work is to investigate the effects of a fault zone during CO<sub>2</sub> injection when the initially dormant fractures in the fault damage zone are geomechanically activated and the petrophysical properties are altered by geomechanical causes. This objective will be achieved using coupled numerical reservoir simulations where we intend to:

- determine the geomechanical response of the fractures in the damage zone of the fault and the alterations to the intrinsic permeability and/or porosity.
- estimate pore pressure variations and underground displacements.
- quantify the extent of CO<sub>2</sub> migration in the reservoir rock and through the fault and its associated fractured damage zone.

## Chapter 2. CO<sub>2</sub> Trapping Mechanisms in Deep Saline Aquifers

Primary and secondary trapping mechanisms can be identified for CO<sub>2</sub> geological storage. Structural/stratigraphic trapping (described in detail in Section 2.1), considered a primary mechanism, refers to the act of containing CO<sub>2</sub> by a geological structure such as a low-permeability confining zone or caprock. This mechanism is vital to prevent any CO<sub>2</sub> leakage and to ensure that other trapping mechanisms can take place (Zhang et al., 2014). The secondary mechanisms are residual trapping (Section 2.2), solubility trapping (Section 2.3), and mineral trapping (Section 2.4).

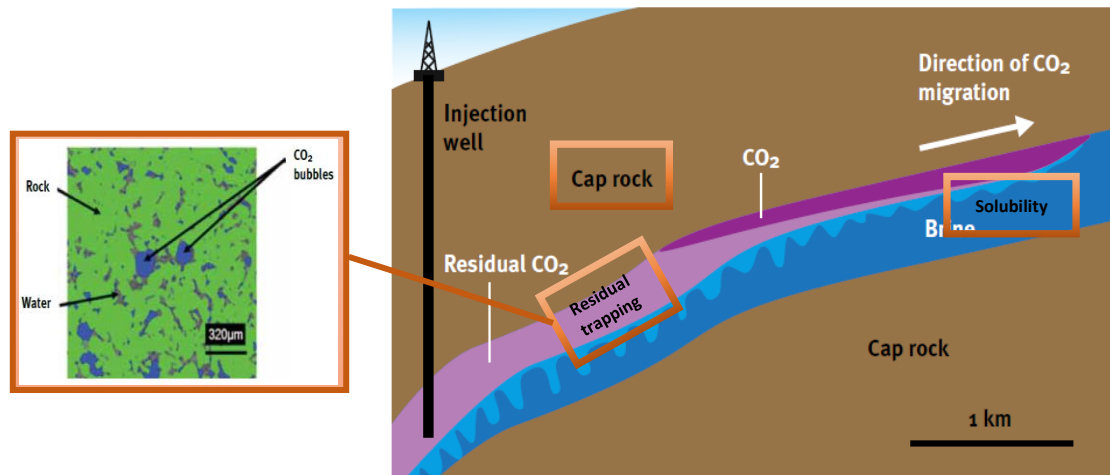


Figure 2.1. A schematic representation of three trapping mechanisms of CO<sub>2</sub> in saline aquifers (Blunt, 2010).

### 2.1. Structural/stratigraphic Trapping

When CO<sub>2</sub> is injected to a geological formation, it migrates upwards due to buoyancy forces until it encounters a low permeability rock or structure that impedes further fluid migration. CO<sub>2</sub> migration is possible because it has a liquid-like density and a gas-like viscosity (Zhang et al., 2014). The density of CO<sub>2</sub> is lower than that of the brine in the storage formation, and its viscosity is about one-tenth of the viscosity of the brine (Blunt, 2010). Possible structural and stratigraphic

traps include caprocks, sealing faults, and unconformities. CO<sub>2</sub> sequestration by this mechanism depends strongly on the sealing integrity of the caprock/fault (Zhang et al., 2014).

## 2.2. Residual Trapping

Residual trapping affects the migration and distribution of CO<sub>2</sub>. Upon initial injection, CO<sub>2</sub> moves through the porous space displacing the brine. When gravity force dominates the flow, brine re-imbibes the pore space, leading to a significant amount of CO<sub>2</sub> becoming trapped as an immobile phase (Zhang et al., 2014) within the pore space of the host rock. In this work, residual gas trapping is modeled with Land's model based on relative permeability curves and hysteresis effects (Land, 1968; Nghiem et al., 2009). The Land's coefficient can be estimated with Equation 2.1 (Nghiem et al., 2009).

$$C = \frac{1}{S_{gt,max}} - \frac{1}{S_{g,max}} \quad 2.1$$

where

$S_{g,max}$ : Maximum gas saturation

$S_{gt,max}$ : Maximum trapped saturation

The residual gas saturation  $S_{gi}^*$  can then be calculated with Equation 2.2.

$$S_{gt}^*(S_{gi}^*) = \frac{S_{gi}^*}{1 + CS_{gi}^*} \quad 2.2$$

where:  $S_{gt}^*$  is the trapped residual oil saturation.

## 2.3. Solubility Trapping

Solubility trapping refers to the dissolution of CO<sub>2</sub> in the brine, which is responsible for a significant portion of CO<sub>2</sub> storage (Nghiem et al., 2009). Once CO<sub>2</sub> dissolves in brine, it will form

a denser phase that will migrate downwards by gravitational segregation (Blunt, 2010). CO<sub>2</sub> solubility in the in-situ brine depends on several factors such as pressure, temperature and salinity (Zhang et al., 2014). Past studies indicate that significant CO<sub>2</sub> solubility in brine takes hundreds or even thousands of years due to its minimal molecular diffusion coefficient (Zhang et al., 2014). In CMG-GEM, gas solubility is modeled as a phase equilibrium process, governed by Henry's law in combination with the Peng-Robinson Equation of State (Nghiem et al., 2009).

#### 2.4. Mineral Trapping

Ions formed by CO<sub>2</sub> dissociation in the brine may react over time with minerals present in the rock. These reactions could be beneficial or deleterious for CO<sub>2</sub> storage. Precipitation reactions that may occur when oxides in the rock dissolve and then precipitate as carbonates reducing porosity and permeability of the rock can help CO<sub>2</sub> trapping (Blunt, 2010; Zhang et al., 2014). Dissolution reactions that may occur if some acid dissolves certain minerals in the rock that will result in the increment of porosity and permeability can facilitate CO<sub>2</sub> migration (Blunt, 2010; Zhang et al., 2014). Significant mineral trapping occurs at a geological timescale. Meager reaction rates result in prolonged precipitation/dissolution processes. Reaction rates depend on pressure, pH, temperature and concentration of species influence reaction rate of minerals (Zhang et al., 2014).

### Chapter 3. Fault Structure and Effects on CO<sub>2</sub> Sequestration

A fault is a displacement zone between two blocks of rock. Faults of tectonic origin can generally be classified as normal faults when they are formed due to the extension of the rock, as inverse faults when they are the result of compressive forces and strike-slip faults that are also formed due to compressive forces that displace horizontally nearly parallel to the force direction (Press et al., 2004). Figure 3.1 is a representation of these three fault types; some fault-related terminology is also included.

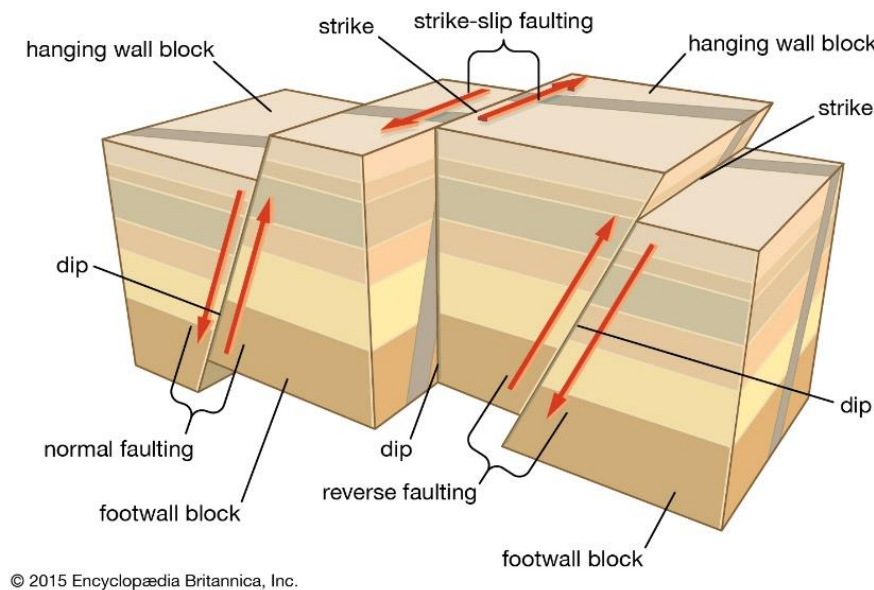


Figure 3.1. Generic classification of faults: normal, reverse and strike-slip faults. (Britannica, 2018). For a dipping fault, the Hanging Wall is the block positioned over the fault; the Foot Wall is the block positioned under it. Fault strike is the direction of a line created by the intersection of a fault plane and a horizontal surface, 0° to 360°, relative to North.

The structure of a fault zone depends on tectonics, depth of the formation, the magnitude of displacement and fluid flow. The classical structure of a fault comprises a fault core and a damage zone that surrounds it. In low porosity rocks, such as those rich in clay, the core is constituted by cohesive fine-grained materials resulting from the faulting process such as cataclasite, gouge, and ultracataclasite, and the fractured damage zone consists of several scale fractures distributed along

the fault (Faulkner et al., 2010). Fractures in the damage zone in low permeability host rocks are dilatant (Blenkinsop, 2007). Faults in high porosity rocks, such as sandstones, are composed of cores with incohesive materials, and their damage zones show deformation bands that propagate resulting in high permeability surfaces (Faulkner et al., 2010). Figure 3.2 shows the classical structure of a fault in a low porosity rock that defines a fault core and a damage zone that surrounds the core.

The density of fractures in low permeability host rocks is a frequent topic of study. It has been found that the fracture density usually decreases exponentially with distance from the fault core. In high permeability rocks, the microfractures caused by the deformation bands often show no variation with distance along the damage zone (Anders et al., 1994). Damage zone widths have a close relationship with fault displacement. Past studies show that the growth in damage zone width will increase with displacement. However, after some hundreds of meters of displacement, the width-to-growth ratio decreases (Faulkner et al., 2010).

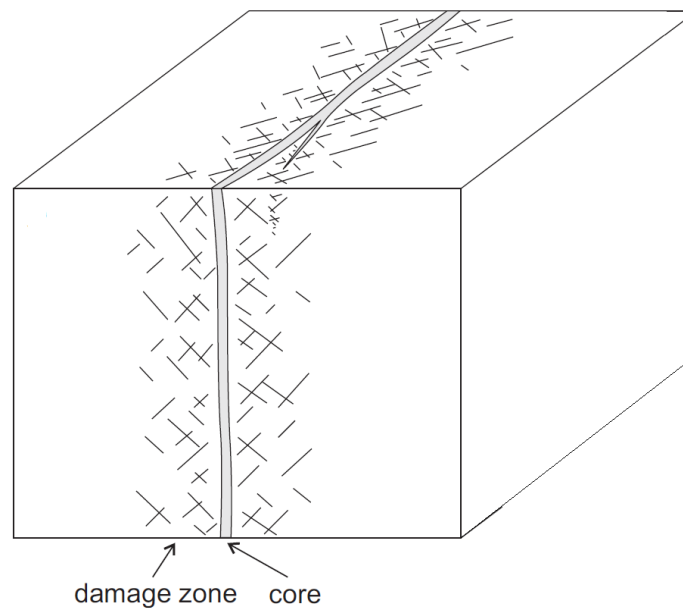


Figure 3.2. Simplified scheme of a typical fault structure, where there are a fractured damage zone and a high-strain core (Childs et al., 2009).

### 3.1. Fault Permeability

Flow barriers can be formed across faults, whereas flow conduits can be formed along them. The ability of a fault to transmit fluids depends on several factors that include the permeability of fracture zone, the permeability of the host rock, the mechanical properties of the host rock, heterogeneity, mineralization, pressure gradients and fracture geometries (Nicol et al., 2017). When faults are present near a CO<sub>2</sub> injection site, variations in pressures, temperatures and injection rates influence some of these factors through time. For instance, CO<sub>2</sub> injection causes pore pressure increments and a reduction in effective stresses, thereby causing fracture apertures and/or fault slip or generating new fractures of hydraulic origin, all of which could compromise storage integrity and promote CO<sub>2</sub> leakage (Nicol et al., 2017).

Several observations determined that fracture permeabilities may change with depth when geochemical interactions of dissolution or precipitation occur. Also, when geomechanical forces increase, fracture permeabilities follow suit due to fracture opening (Nicol et al., 2017). When these processes that influence fracture aperture cease, fractures rarely close completely or return to their initial permeabilities. In other words, fracture permeabilities that are modified due to geochemistry and/or geomechanics undergo irreversible alterations. Particularly on sub-geological time scales, self-healing of fractures due to mineral precipitation is not expected on storage operations where CO<sub>2</sub> migrates through faults (Nicol et al., 2017). When referring to fracture closure after geomechanical events subside or conclude, fracture permeabilities will not have the same initial value due to misalignment of rough surfaces (Nicol et al., 2017). These fundamental concepts are required for this work, and they will be accounted for and explained in the following sections.



### 3.2. CO<sub>2</sub> Leakage through Faults

If the fault structure is a conductive pathway, then CO<sub>2</sub> can migrate through it if the buoyancy pressure exceeds the capillary entry pressure (Smith et al., 2011). CO<sub>2</sub> leakage through faults may be hazardous and detrimental, especially when there are freshwater reservoirs in the upper formations. However, in some cases where no environmental damage is caused, it would be plausible to design CO<sub>2</sub> storage sites that dissipate CO<sub>2</sub> injection volumes to other reservoir layers through the fault zones (Smith et al., 2011). Besides environmental concerns, faults that were formed before CO<sub>2</sub> injection, or the reactivation of faulted zones during the injection period can modify storage capacity, maximum injection pressures and rates, and caprock integrity (Nicol et al., 2017).

In general, CO<sub>2</sub> may leak along the fault zone or may make its way across the fault. Clay-rich (low-permeability) formations may impede flow across the fault, but the congregation of the fractures in the damage zone can promote flow along the fault. Along-fault migration of CO<sub>2</sub> is more significant where there is a higher density of small-scale fractures, a more extensive or more connected fracture network and/or a critically stressed fault (Figure 3.3). Previous flow simulation results also show that compartmentalized low permeability reservoirs promote pressure buildup allowing the flow of CO<sub>2</sub> along the fault (Nicol et al., 2017). Research has been done to evaluate the pressure variations during fault leakage in compartmentalized reservoirs (Mosaheb et al., 2017a, 2017b, 2018). In along-fault flow, fracture connectivity is determinant for hydraulic conductivity. For instance, two different fault zones may have a similar fault structure, but only the one with sufficiently connected high-permeability pathways will allow fluid flow (Nicol et al., 2017).

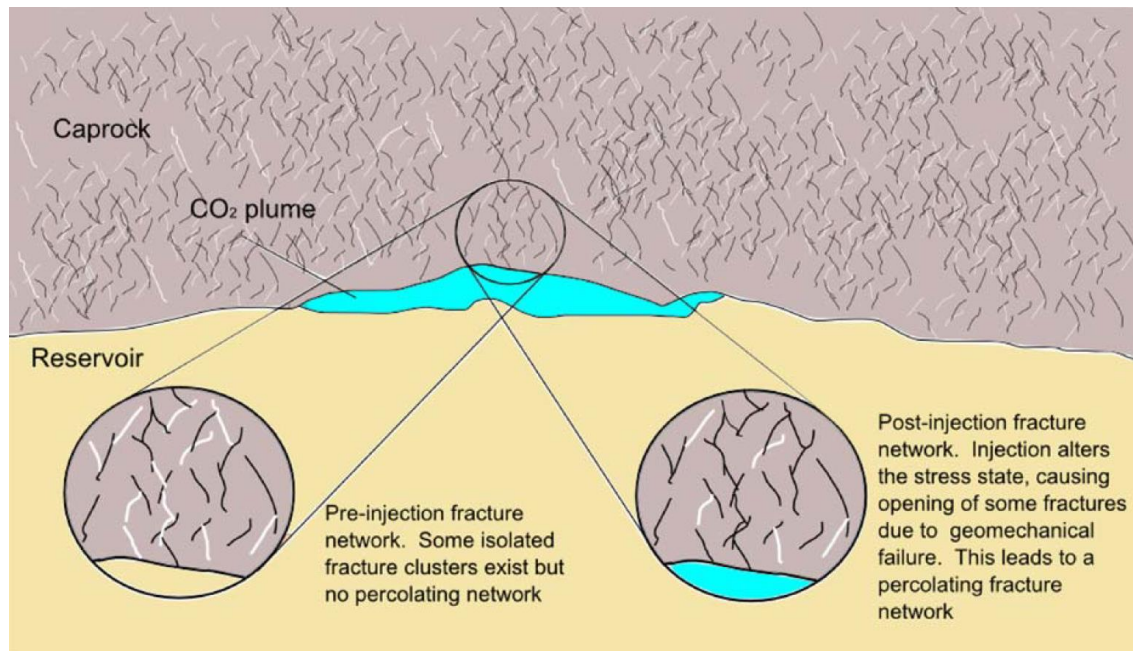


Figure 3.3. Possible paths of CO<sub>2</sub> migration due to the formation of fracture networks as a result of injection pressure in a naturally fractured caprock (Smith et al., 2011).

## **Chapter 4. Multiphase Fluid Flow coupled with Geomechanics for CO<sub>2</sub> storage in Saline Aquifers**

In general, geomechanical studies help to explain phenomena such as reservoir compaction, subsidence, rock failure, pore collapse or wellbore stability (Tran et al., 2004). Geomechanics applied specifically to the modeling of CO<sub>2</sub> sequestration helps explain vertical displacement, the opening of caprock fractures or the reactivation of pre-existing fractures, and notable seismic events (Varre et al., 2015).

Four different ways in which caprocks can fail have been identified: diffusive loss through the caprock, leakage through pore spaces when the capillary breakthrough pressure has been exceeded, leakage through faults or fractures, and leakage through wells that are degraded or inappropriately abandoned. These leakage mechanisms are reviewed by Zhang et al. (2014). Of these leakage pathways, the principal concern when evaluating caprock integrity often involves leakage through faults or fractures (Yudhowijoyo et al., 2018). Induced fractures and reactivated fractures have a negative impact on the integrity of the primary trapping mechanism, and CO<sub>2</sub> may escape through the fractures and reduce storage capacity. It is during the injection period that the fluid pressures are highest and that the CO<sub>2</sub> is most mobile and prone to escape. To allow large-scale storage without fracturing the rock or activating dormant fracture and faults during this period, both of which could cause encroachment into freshwater aquifers, it is essential to avoid significant pressure increases at the well and in the underground storage formation. Over time, the structural integrity improves due to CO<sub>2</sub> dissolution, precipitation or capillary trapping (Blunt, 2010).

The potential of leakage will depend on external loads, formation types and rates or pressures of CO<sub>2</sub> injection. Tran et al. (2009) presented an approach to predict possible leakage during CO<sub>2</sub> injection into an aquifer by coupling reservoir fluid flow with a geomechanical module in the

CMG-GEM simulator (CMG, 2017). Furthermore, the authors applied a modified Barton-Bandis model (Bandis et al., 1983) to calculate fracture permeability so that CO<sub>2</sub> leakage through the caprock towards the overburden could be modeled.

The inclusion of geomechanics in the reservoir simulator can be achieved by three methods. The fully coupled model calculates fluid flow and deformation parameters simultaneously. In the iterative method, fluid flow parameters are calculated first and then sent to the geomechanical module to calculate stresses, strains and deformation vectors that are sent back to the reservoir simulator. Results from the geomechanical calculations are sent back to the reservoir simulator in the form of coupling variables: porosity and permeability. These coupling variables are used to obtain new pressures and temperatures that are input data of the geomechanical module. This loop process iterates until reaching convergence (Tran et al., 2004). Figure 4.1 explains the iterative process of a simulation coupled with geomechanics. The explicit coupling performs the geomechanical calculations once, but these results are not input data of the reservoir simulator until the next time step. Regarding efficiency and flexibility, the iterative method is the best choice. It also demonstrated comparable accuracy when compared to the fully coupled method, where the governing equations of fluid flow and mechanical displacements are solved simultaneously each time step (Tran et al., 2004).

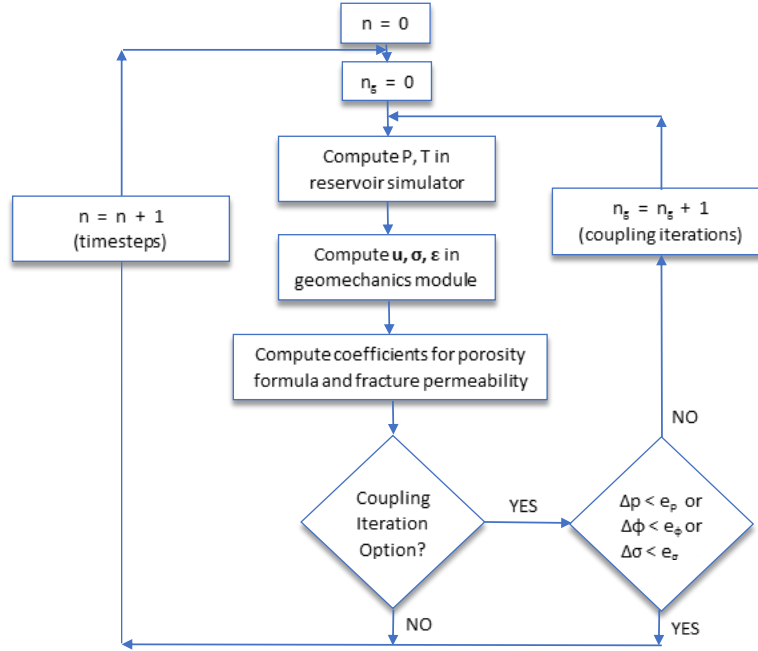


Figure 4.1. Flowchart for iterative coupling of fluid flow simulation with geomechanics (Tran et al., 2009).

#### 4.1. Barton-Bandis Model for Fracture Permeability

In a conventional iterative coupling simulation with geomechanics, porosity and permeability of the rock are the parameters that transfer information from the geomechanical module to the flow simulator. When working with CO<sub>2</sub> leakage, there is the need to include fracture permeability for more accurate modeling. Fracture permeability appears when the rock cracks because the material strength has been surpassed by internal pore pressure and particle bonding is no longer possible.

The Barton-Bandis model (Figure 4.2) is used to estimate fracture permeability with variations in normal fracture effective stress  $\sigma'_n$  that is equivalent to the minimum effective stress (Bandis et al., 1983; CMG, 2017; Tran et al., 2009). Initially (point A), the rock is either non-fractured or includes dormant fractures. Fractures become transmissible to flow once a threshold normal effective stress (point B) is reached. When this stress is reached in a suitably brittle rock, the fracture permeability increases instantaneously to a maximum fracture permeability or hydraulic

fracture permeability,  $k_{hf}$  (point C). If the pore pressure reduces, the normal effective stress increases, and as long as  $\sigma'_n$  is less than zero the fracture permeability remains at  $k_{hf}$  (path DCE). When  $\sigma'_n$  is greater than the fracture opening stress  $f_{rs}$  and greater than zero, fracture permeability reduces to fracture closure permeability  $k_{ccf}$  (point F). If  $\sigma'_n$  keeps increasing, the permeability of the fracture reduces asymptotically following the Barton-Bandis model to a residual value of fracture closure permeability  $k_{rcf}$  (path FG) (Bandis et al., 1983; CMG, 2017). If  $\sigma'_n$  reduces thereafter, fracture permeability will reversibly follow the path GFED (CMG, 2017).

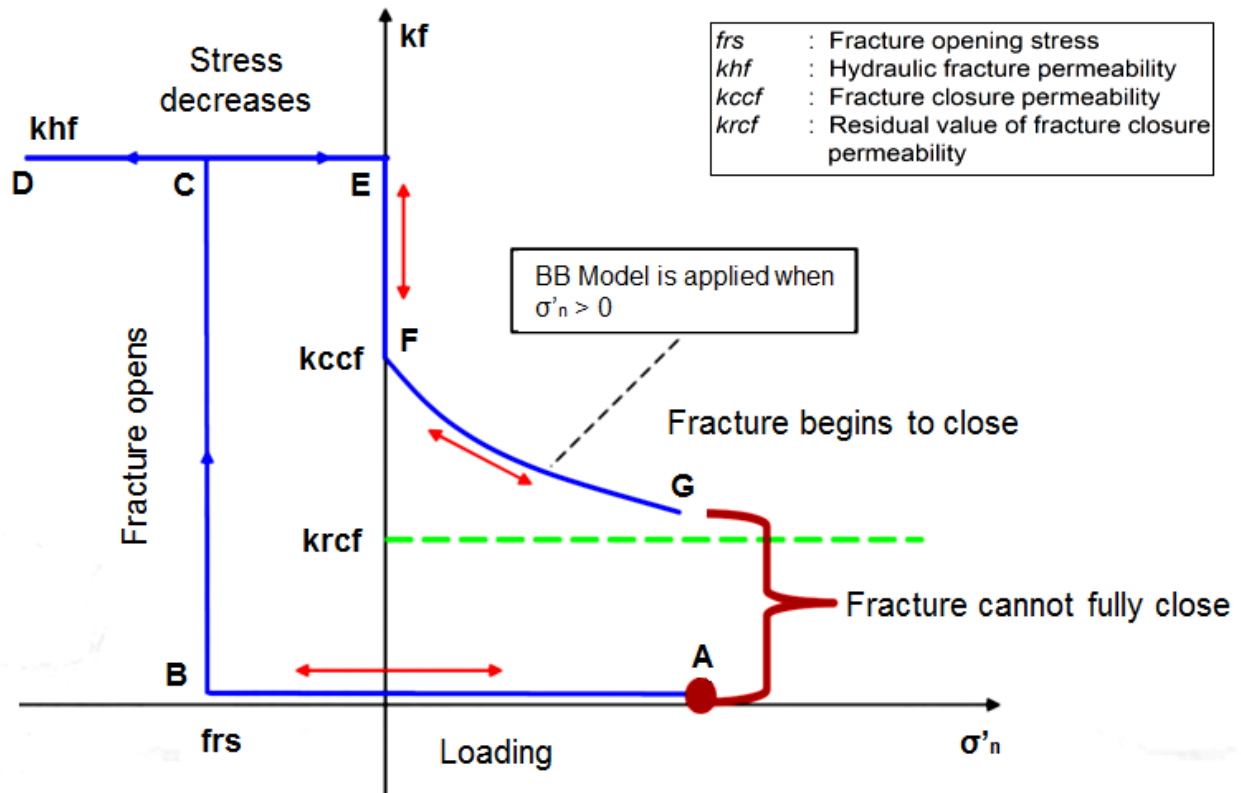


Figure 4.2. Fracture permeability based on modified Barton-Bandis model (Tran et al., 2009).  $\sigma'_n$  is the normal fracture effective stress and  $k_f$  the fracture permeability. Point A represents the initial conditions. Fracture permeability remains constant with the reduction of  $\sigma'_n$  until point B, the threshold value. When  $\sigma'_n$  reduces to the threshold value, permeability increases to the hydraulic fracture permeability. As soon as  $\sigma'_n$  increases to a value higher than zero, permeability reduces to a fracture closure permeability that is always higher than the initial fracture permeability. If  $\sigma'_n$  continues increasing, permeability is calculated by the Barton-Bandis model (path FG).

The original Barton-Bandis model (Bandis et al., 1983) is an empirical failure criterion that relates shear strength to the normal stress, and it is expressed in Equation 4.1.

$$\tau = \sigma_n \tan \left[ \varphi_b + JRC \log_{10} \left( \frac{JCS}{\sigma_n} \right) \right] \quad 4.1$$

where:

$\tau$ : Shear strength (psi)

JRC: Joint roughness coefficient

$\sigma_n$ : Normal fracture stress acting on the surface of the rock joint (psi)

JCS: Joint compressive strength (psi)

$\varphi_b$ : Basic angle of internal friction of the slip surface

The fracture permeability  $k_f$  (md) can be calculated by (CMG, 2017):

$$k_f = kccf \left( \frac{e}{e_0} \right)^4 \geq krcf \quad 4.2$$

where:

$kccf$ : Fracture closure permeability (md)

$krcf$ : Residual value of fracture closure permeability (md)

$e_0$ : Initial fracture aperture (Ketzer et al.)

The fracture aperture  $e$  is function of the minimum effective stress, fracture closure permeability, residual fracture permeability, initial fracture aperture, and initial normal fracture stiffness  $kni$ .

$$e = e_0 - V_j \quad 4.3$$

$$V_j = \frac{\sigma'_n}{kni + \sigma'_n / V_m} \quad 4.4$$

$$V_m = e_0 \left[ 1 - \left( \frac{krcf}{kccf} \right)^{1/4} \right] \quad 4.5$$

#### 4.2. Fault Influence on CO<sub>2</sub> geological storage

Fault zones have great importance on the risk evaluation of CO<sub>2</sub> leakage since they may behave as conduits of CO<sub>2</sub> migration. Where fault zones have a lower permeability related to the host rock, they can behave as a seal that impedes lateral fluid flow. However, in tight rocks fault zones may have higher permeabilities and behave as fluid conduits for the upward migration of CO<sub>2</sub> (Cilona et al., 2015). The typical hydrogeological structure of a clastic rock consists of a fault core and damage zones, as shown in Figure 1.2. Fault cores have very low permeabilities in brittle clastic rocks due the accumulation of displaced material causing a reduction of grain size, permeability, and porosity. In contrast, the surrounding damaged zone has considerably greater permeability than the fault core and the surrounding unfractured zone due to the presence of complex systems of natural fractures. The damage zone is also more extensive than the fault core, which makes this zone hydraulically more important in the contribution of bulk permeability (Loveless et al., 2014).

Therefore, vertical faults intersecting the aquifer formations near the injection site could cause CO<sub>2</sub> leakage through natural fractures in their damage zones (Liu et al., 2010). Likewise, dormant fractures in the structure of non-leaking zones can be geomechanically and hydraulically activated by the CO<sub>2</sub> injection and provide preferential leakage routes. This effect is exacerbated as the CO<sub>2</sub> plume approaches the fault structure. Additionally, Huo et al. (2010) showed that natural fractures could facilitate horizontal displacement of the CO<sub>2</sub> in the saline aquifer resulting in a plume with a greater extent, which could significantly alleviate pressure buildup.



## **Chapter 5. Model Validation: Fluid Flow Simulation Coupled with Geomechanics**

This Chapter presents the validation of the simulation model developed by Tran et al. (2009) performed with a two-dimensional reservoir model using CMG-GEM (2017) to show the effects of geomechanics on CO<sub>2</sub> sequestration in an aquifer. The reservoir has 411 discretizations in the horizontal direction, and 33 in the vertical. The model has two caprock layers above the reservoir. The fluid flow comprises CO<sub>2</sub> and saline water. The depth of the top layer of the reservoir is 7425 ft. No geochemical or mineral reactions were modeled, neither was water vaporization. The permeability in x-, y-, and z-direction ( $k_x$ ,  $k_y$ , and  $k_z$ ) in different zones is shown in Figure 5.2. The vertical to horizontal permeability ratio in all cases is 1:4. The low vertical permeability of 2.5E-08 md in the shale caprocks ensures practically no fluid exchange between zones. A constant porosity of 0.13 is considered for all the zones. The reservoir is constrained at the bottom and sides and allows the top to move freely. Additional input parameters are shown in Table 5.1 and 5.2, and the relative permeability curves used for this model are presented in Figure 5.1.

For this model, CO<sub>2</sub> is injected for the first five years at a rate of 3,500,000 ft<sup>3</sup>/day. Figure 5.3 shows the minimum horizontal effective stress at the center of caprock-2 at different times for the validation model and the results obtained in the present validation. It should be noted that the results do not show a perfect match because (Tran et al., 2009) simulated the model using CMG-GEM v.2009, while this model is reproduced and simulated in CMG-GEM v. 2017, in this last version the Barton-Bandis model presented in Section 4.1 was modified and it is different to the Barton-Bandis model in CMG-GEM v.2009. A profile of vertical displacements of Caprock 2 is shown in Figure 5.4 for comparison at various times. Before the crack opening at 152 days, and when the crack opens at the 213 days, the trend in the curve displacement vs. distance is similar.

However, after the crack opening, the displacement has less bending when compared to the earlier times.

Table 5.1. Parameters of the injection well used for the validation of the investigation performed by Tran et al. (2009).

|  |   |
|--|---|
| <b>Grid blocks well perforations (I, J, K)</b>     | (51, 1, 30) (51, 1, 31) (51, 1, 32) (51, 1, 32) |
| <b>Injection duration</b>                          | 5 years   |
| <b>CO<sub>2</sub> mole fraction</b>                | 1   |
| <b>Maximum BHP (psi)</b>                           | 7500  |
| <b>Maximum injection rate (ft<sup>3</sup>/day)</b> | 3,500,000                                       |

Table 5.2. Geomechanical rock properties used in the validation model (Tran et al., 2009).

|   |        |
|---|--------|
| Young modulus (kPa)                                     | 5E6    |
| Poisson's ratio   | 0.25   |
| <b>Barton-bandis model for Caprock 1 and 2</b>          |        |
| Initial fracture aperture (Ketzer et al.)               | 6.5E-5 |
| Initial normal fracture stiffness (psi/ft)              | 3.0E-6 |
| Fracture opening stress (psi)                           | 0      |
| Hydraulic fracture permeability, (md)                   | 35     |
| Residual value of fracture closure permeability, (md)   | 5      |
| <b>Initial stress distribution</b>                      |        |
| X-direction effective stress (psi)                      | 500    |
| Y-direction effective stress (psi)                      | 500    |
| Z-direction effective stress (psi)                      | 1000   |
| X-Y plane shear stress (psi)                            | 0      |
| Y-Z plane shear stress (psi)                            | 0      |
| X-Z plane shear stress (psi)                            | 0      |
| <b>Linear variation in stress components with depth</b> |        |
| X direction effective stress gradient (psi/ft)          | 0.4628 |
| Y direction effective stress gradient (psi/ft)          | 0.4628 |
| Z direction effective stress gradient (psi/ft)          | 0.9256 |
| X-Y plane shear stress gradient (psi)                   | 0      |
| Y-Z plane shear stress gradient (psi)                   | 0      |
| X-Z plane shear stress gradient (psi)                   | 0      |

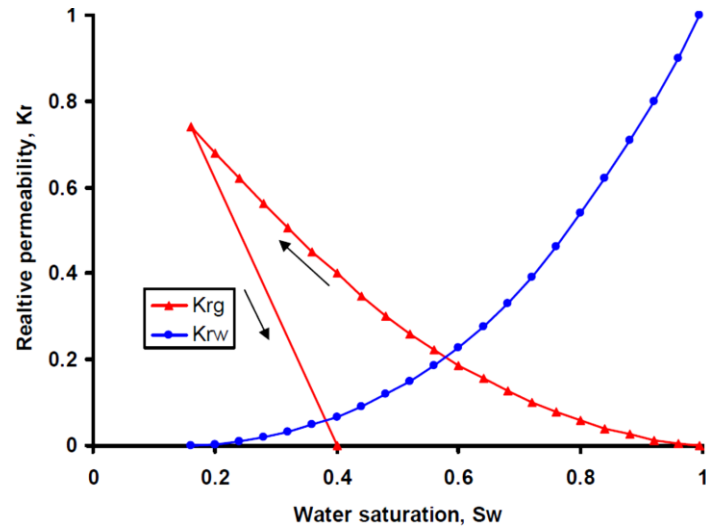


Figure 5.1. Gas and water relative permeability curves used in the validation model (Tran et al., 2009).

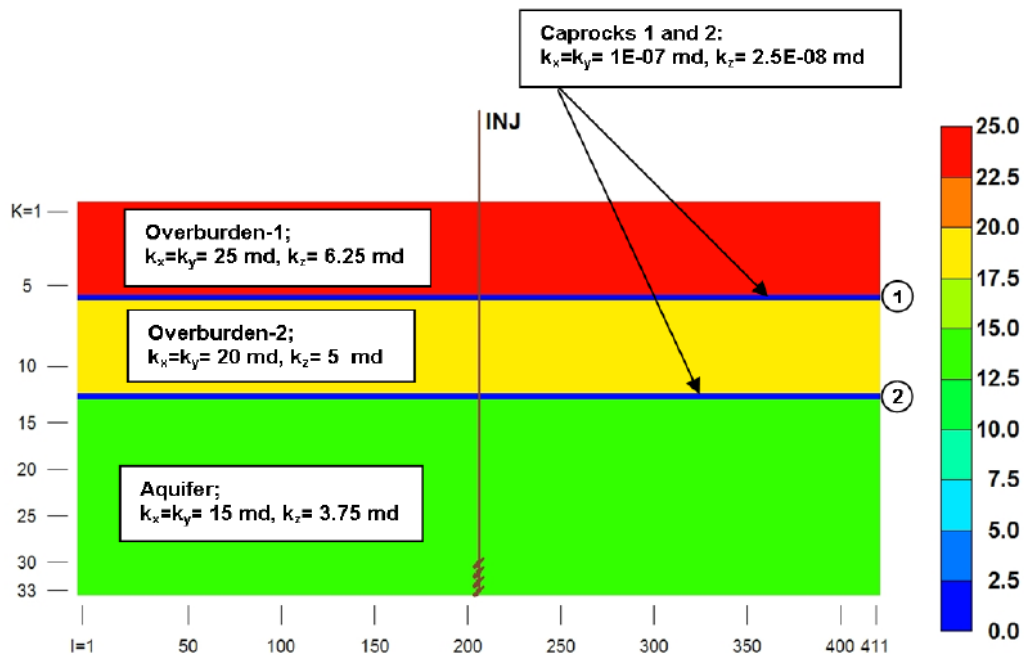


Figure 5.2. Reservoir description for the validation model: horizontal and vertical permeability in the aquifer, caprocks, overburden-1, and overburden-2 (Tran et al., 2009).

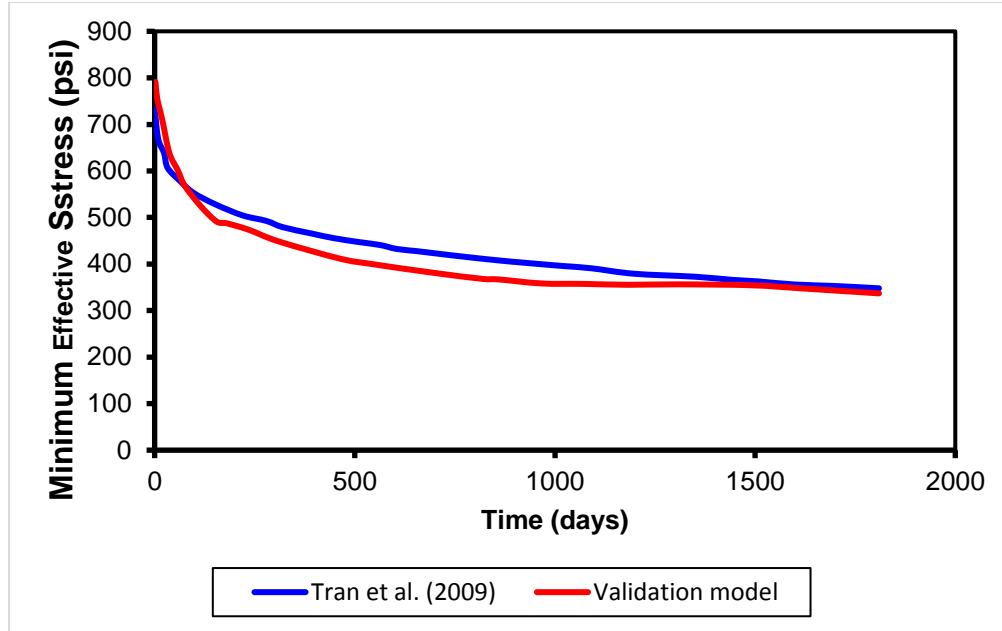


Figure 5.3. Normal fracture effective stress at center of Caprock 2 and the center of the base of the Overburden 2. The minimum horizontal stress profiles show the fractures open after 213 days (0.58 years) of injection.

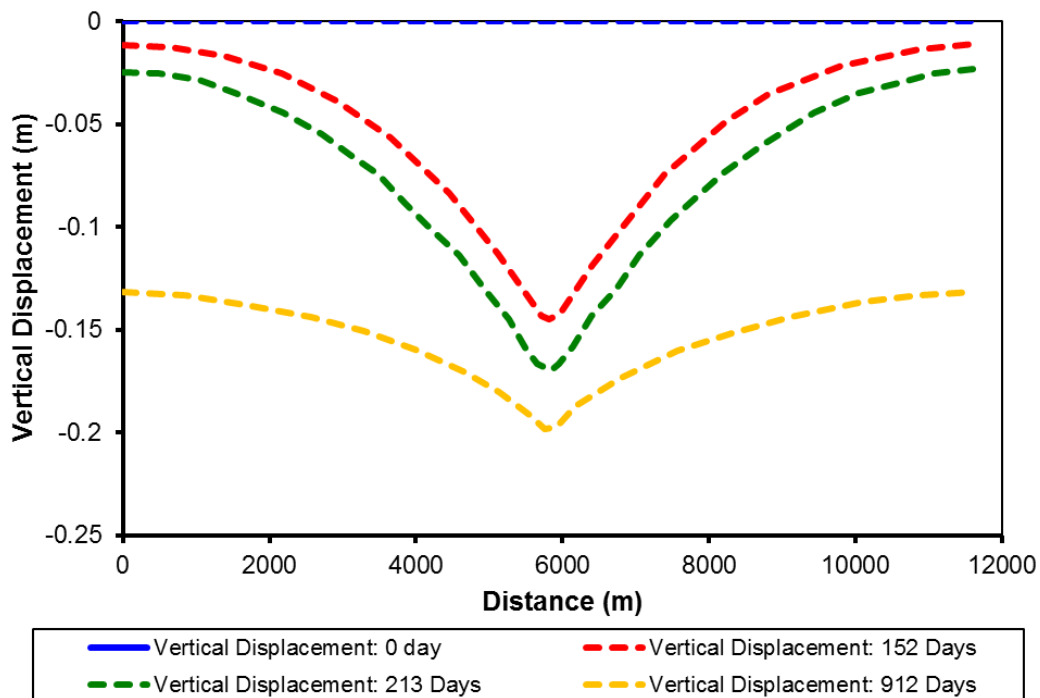


Figure 5.4. Vertical displacement of Caprock 2. Vertical displacement increases gradually during CO<sub>2</sub> injection. After four years of injection, the vertical displacement is approximately 0.2 m.

Figure 5.6 shows the comparison of the CO<sub>2</sub> saturation profiles for the present validation model and the results obtained by (Tran et al., 2009). The gas-saturation distribution in the system is shown four years after injection begins. Note that for this specific time Caprock 1 was also fractured.

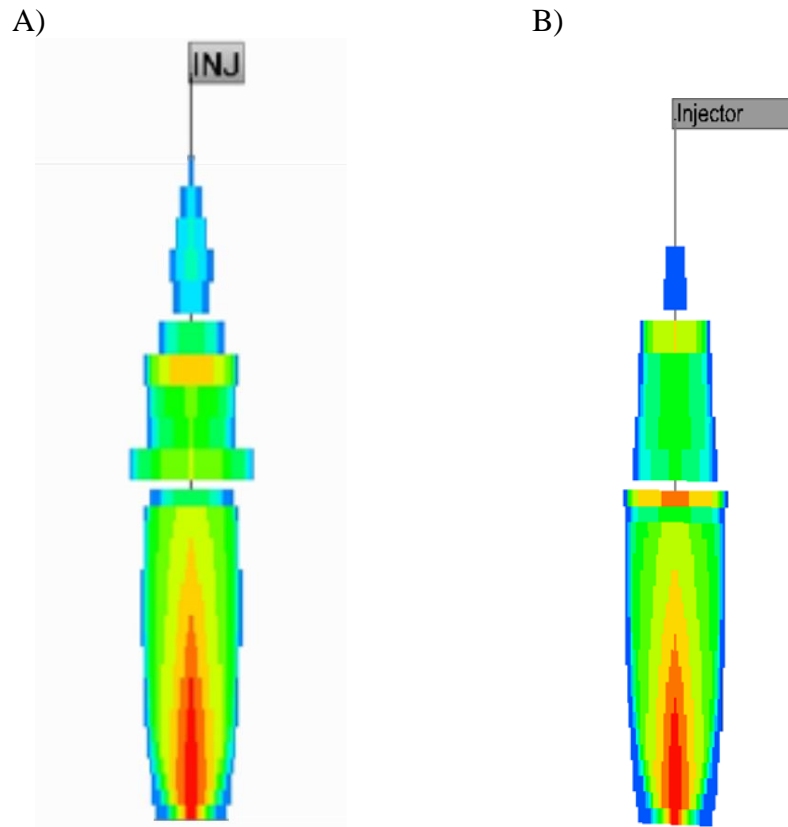


Figure 5.6. A) Contour map of CO<sub>2</sub> gas saturation distribution after four years of injection presented by (Tran et al., 2009). B) Contour map of CO<sub>2</sub> gas saturation distribution after four years of injection obtained by the validation model. It can be observed that fractures in Caprocks 1 and 2 become conductive and allow leakage of CO<sub>2</sub> into Overburdens 1 and 2.

## **Chapter 6. Simulation of a Representative Model with an Idealized Sealing Fault**

This chapter describes a simple geometry simulation model for CO<sub>2</sub> sequestration in a saline aquifer. We use a dual permeability approach to account for the effect of fractures on fluid flow along/up a vertical laterally sealing fault with an impermeable core and a damage zone. Due to the non-conductivity of the fault core we only model up-fault leakage through the damage zone and neglect across-fault leakage. The damage zone is homogeneous and isotropic which includes dormant fractures. It is important to mention that capillary scaling effects have a negligible influence on flow through homogenous damage zones (Zulqarnain et al., 2018), so they are not considered in the simulation. The simulation results are presented in terms of CO<sub>2</sub> gas moles, stress changes, and fracture permeability and porosity alterations for ten years of CO<sub>2</sub> injection. The opening, propagation, and closure of the dormant fractures in the damage zone have been modeled using the Barton-Bandis model.

### **6.1. Model Description**

In this representative model, the vertical fault intersects three geological formations, two of which are sand layers separated by a shale caprock (Figure 6.1). The damage zone, which has a porosity of 8%, is thicker in the lower and upper sandstones than in the shale layer. The initial horizontal and vertical permeability of the damage zone in the sands is 0.65 md, and in the shale formation is 0.1 nd. The permeability of the damage zone can be lower than the permeability of the host sand layers, especially in reservoirs with high confining pressures (Zulqarnain et al., 2018). The damage zone generally has higher permeability than the shale host. However, for simulation purposes and assuming that the damage zone fractures are initially dormant in the shale host, the low permeability of 0.1 nd is considered for the damage zone in the shale layer. Fracture spacing is 5

ft in the X, Y, and Z directions. The maximum CO<sub>2</sub> injection rate is 50,000 ft<sup>3</sup>/day and is maintained for ten years regardless of bottom hole pressure. CO<sub>2</sub> injection occurs from January 2019 to January 2029 from a well located approximately 50 ft from the fault (Figure 6.1).

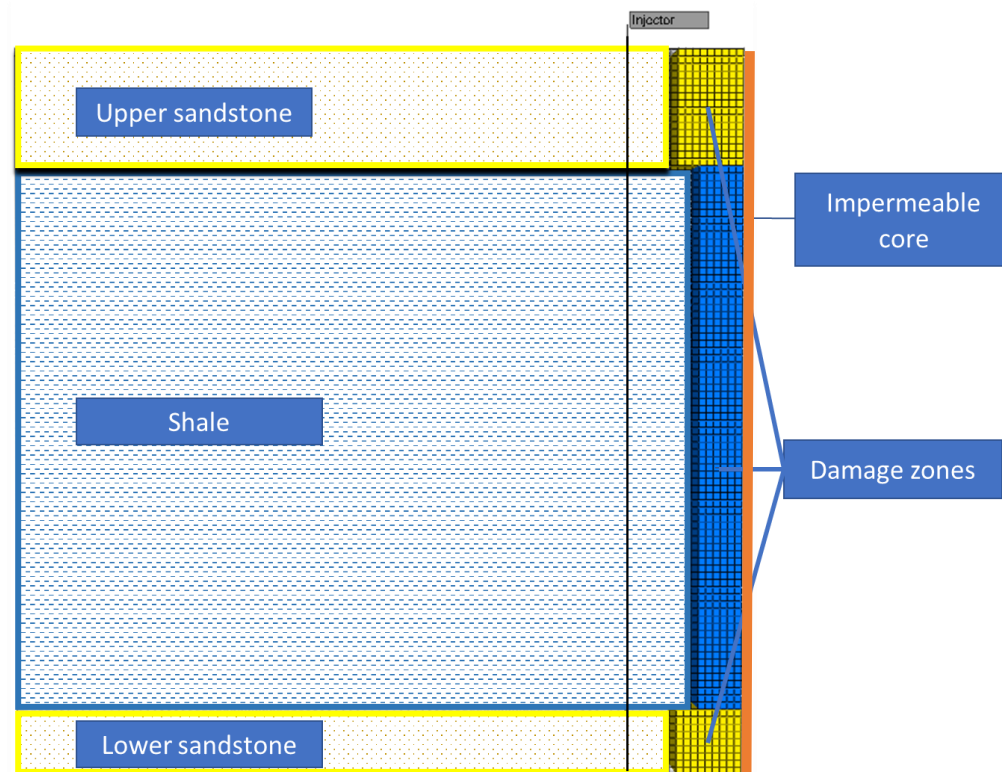


Figure 6.1. Cross-sectional configuration of the simple geometry model.

This model assumes a poro-elastoplastic behavior of the rocks. Therefore, geomechanical calculations are performed according to the Mohr-Coulomb constitutive model. The initial effective horizontal normal stress is 5000 psi, and the effective maximum normal stress is 8500 psi at the top of the model. The stress gradients for the horizontal and vertical directions are 0.879 and 1.075 psi/ft respectively, which match those typically present in deep overpressured tight shale systems (Padmakar, 2013). The Barton-Bandis model is applied only to the fractures in the damage zone, meaning that the permeability changes will be reflected only in this region. Table 6.1 displays the mechanical properties of the formations, and Table 6.2 shows the variables given

as input data for the Barton-Bandis model. Figure 6.2 presents the relative permeability curves used for this model.

Table 6.1. Mechanical properties for the sandstones and the caprock in the simple geometry model (Molina et al., 2017).

|                            | Young Modulus<br>E (psi) | Cohesion<br>C(psi) | Poisson's ratio<br>$\nu$ |
|----------------------------|--------------------------|--------------------|--------------------------|
| Lower and upper sandstones | 7.25E4                   | 1E5                | 0.2                      |
| Shale (caprock)            | 3.625E6                  | 1E5                | 0.3                      |

Table 6.2. Barton-Bandis model parameters applied only for fracture permeability calculations in the damage zones of the simple geometry model. Initial fracture aperture and initial normal fracture stiffness were obtained from Ketzer et al. (2012), and the other four parameters shown in the table were assumed.

|  |        |
|--|--------|
| Initial fracture aperture                            | 6.5E-5 |
| Initial normal fracture stiffness (psi/ft)           | 3.22E6 |
| Differential fracture opening stress (psi)           | -300   |
| Hydraulic fracture permeability (md)                 | 1000   |
| Fracture closure permeability (md)                   | 1000   |
| Residual value of fracture closure permeability (md) | 50     |

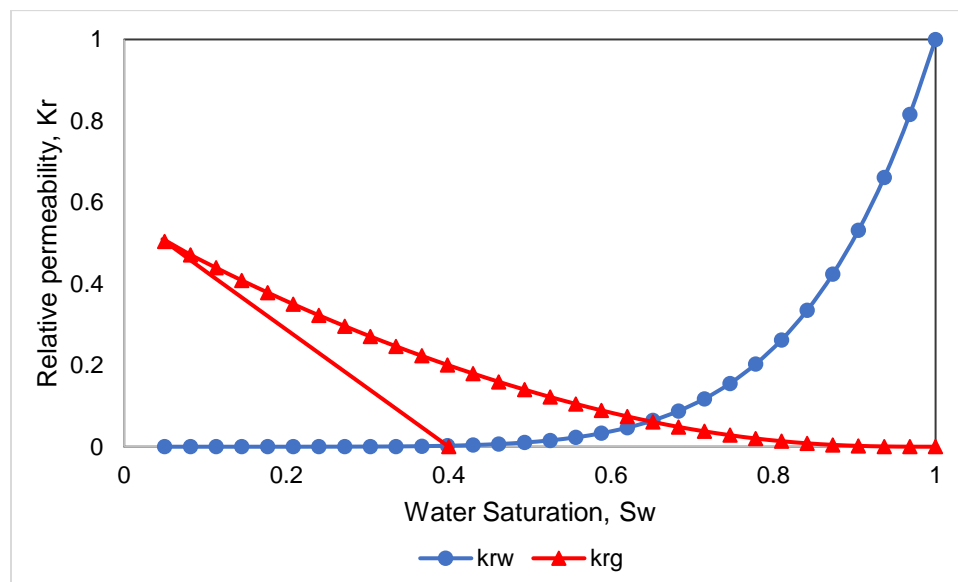


Figure 6.2. Gas and water relative permeability curves in the Mt. Simon sandstone in Western Ohio used for the simple geometry model (Krevor et al., 2012).



## 6.2. Results

As anticipated, the inclusion of geomechanics in the simulation resulted in the opening of the dormant fractures in the damage zone causing the loss of caprock integrity and, therefore, the leakage of CO<sub>2</sub>. After 120 days of injection, CO<sub>2</sub> starts leaking through the fractures of the damage zone that begin to open when the differential fracture opening stress exceeds 300 psi, as specified in the Barton-Bandis input variables. After 851 days of injection, CO<sub>2</sub> starts to flow from the fractures into the upper sand. Figures 6.3 and 6.4 present the CO<sub>2</sub> plume migration and distribution contour maps through the matrix and fractures at different times during injection. The main paths for CO<sub>2</sub> leakage are the geomechanically activated fractures present in the damage zone. CO<sub>2</sub> flow through the matrix of the damage zone is negligible compared with flow through the fractures.

Figure 6.5 shows the contour maps of effective minimum horizontal stresses at different times during CO<sub>2</sub> injection. It can be observed that the effective normal stress will reduce as the pore pressure increases due to CO<sub>2</sub> injection. The most dramatic stress changes occur in the damage zone in the shale, if compared with the damage zone in the sandstones. At the bottom of the damage zone in the shale caprock, the minimum horizontal stress reduction after the injection period is about 3400 psi. The minimum horizontal stress of the damage zone located at the base of the upper sandstone decreases by approximately 1100 psi. Similar behavior is observed in the base of the damage zone in the lower sandstone where the normal effective stress reduction is about 1000 psi.

The implementation of the Barton-Bandis model and the iterative geomechanical coupling allowed the simulation to change the fracture permeability in the damage zone. Figure 6.6 depicts the fracture permeability in the damage zone after one year of CO<sub>2</sub> injection and at the end of the injection period. Initially, the fracture permeability is 0.1 nd, but after one year there is a fracture permeability change from the bottom of the damage zone to the mid-height of the shale. In this

zone, the fracture permeability immediately increases to 1000 md. At the end of the injection period the fracture permeability in all the extension of the damage zone in the shale changes to 1000 md. Porosity changes, computed on the basis of porosity coefficients which were estimated in the geomechanics module in a previous time step, are also calculated as a function of pressure, temperature and total mean stress (CMG, 2017). Figure 6.7 shows the porosity in the fractures of the damage zone at different times. The results show that porosity increases from 8% to values in the range of 9.5 to 10.3%.

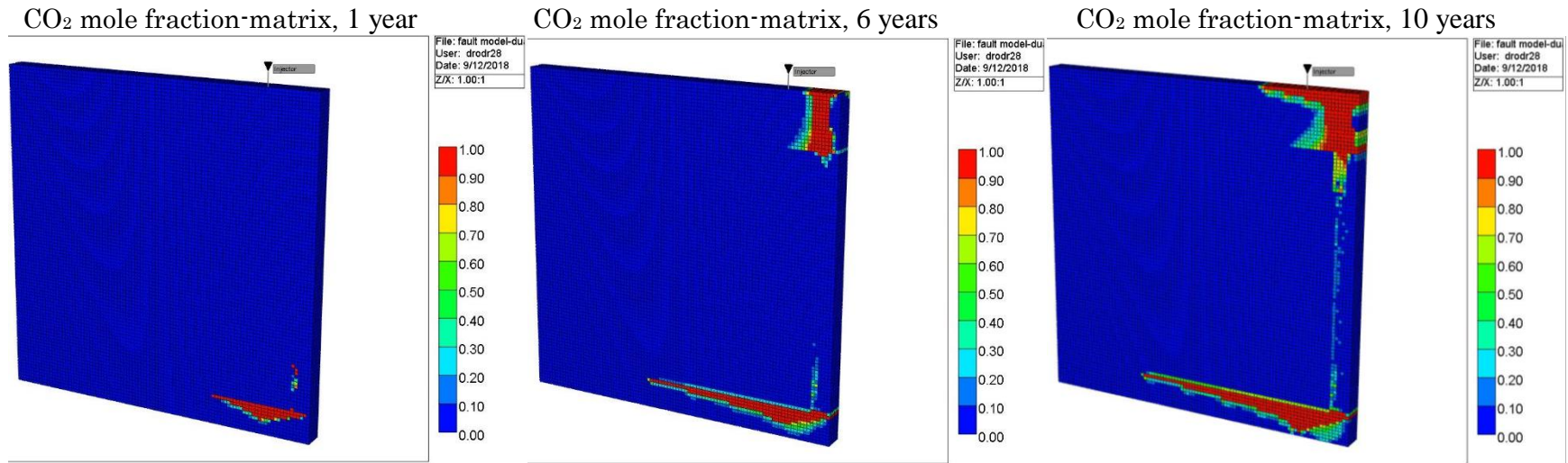
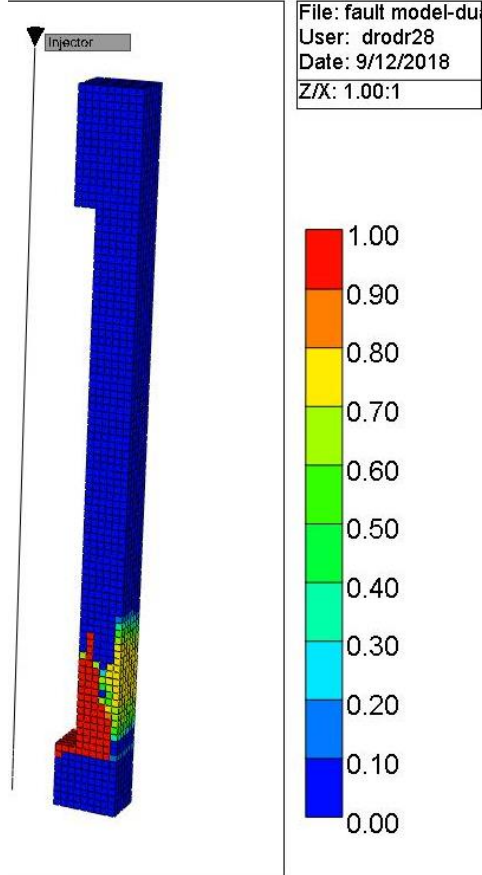
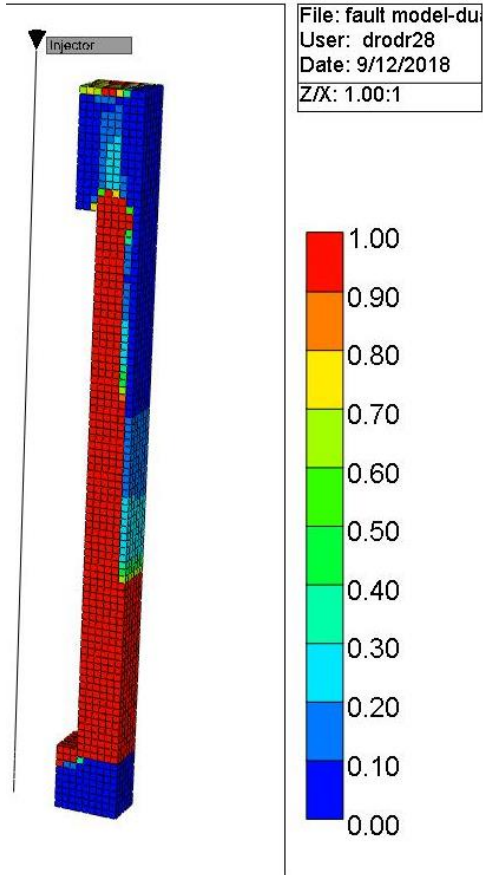


Figure 6.3. CO<sub>2</sub> mole fraction in the matrix for the dual-permeability fault model with simple geometry. After six years of injection, a considerable amount of CO<sub>2</sub> saturated the vicinity of the fault in the upper sandstone. The lack of continuity of CO<sub>2</sub> plume between the sands is because the main conduit for fluid migration is the opened fractures in the damage zone. After ten years of injection, more grid blocks in the sands are saturated by CO<sub>2</sub>.

CO<sub>2</sub> mole fraction-fractures, 1 year



CO<sub>2</sub> mole fraction-fractures, 6 years



CO<sub>2</sub> mole fraction-fractures, 10 years

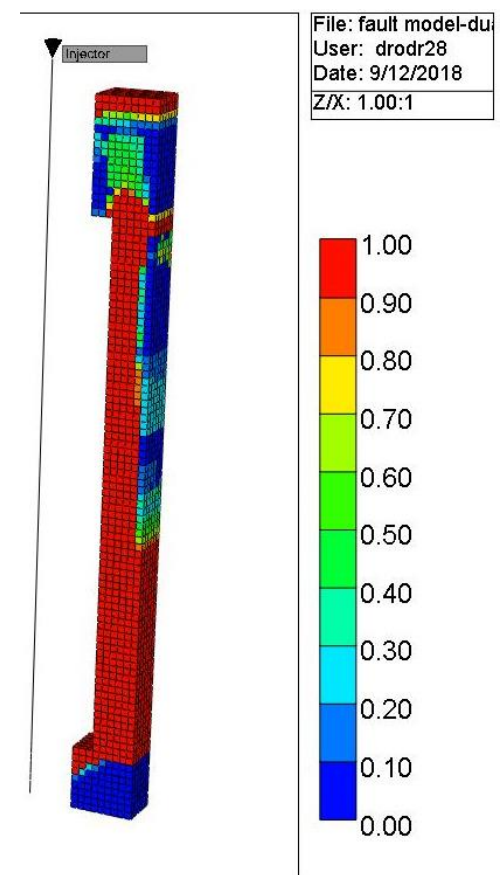


Figure 6.4. CO<sub>2</sub> mole fraction in the fractures of the damage zone for the dual-permeability fault model with simple geometry.

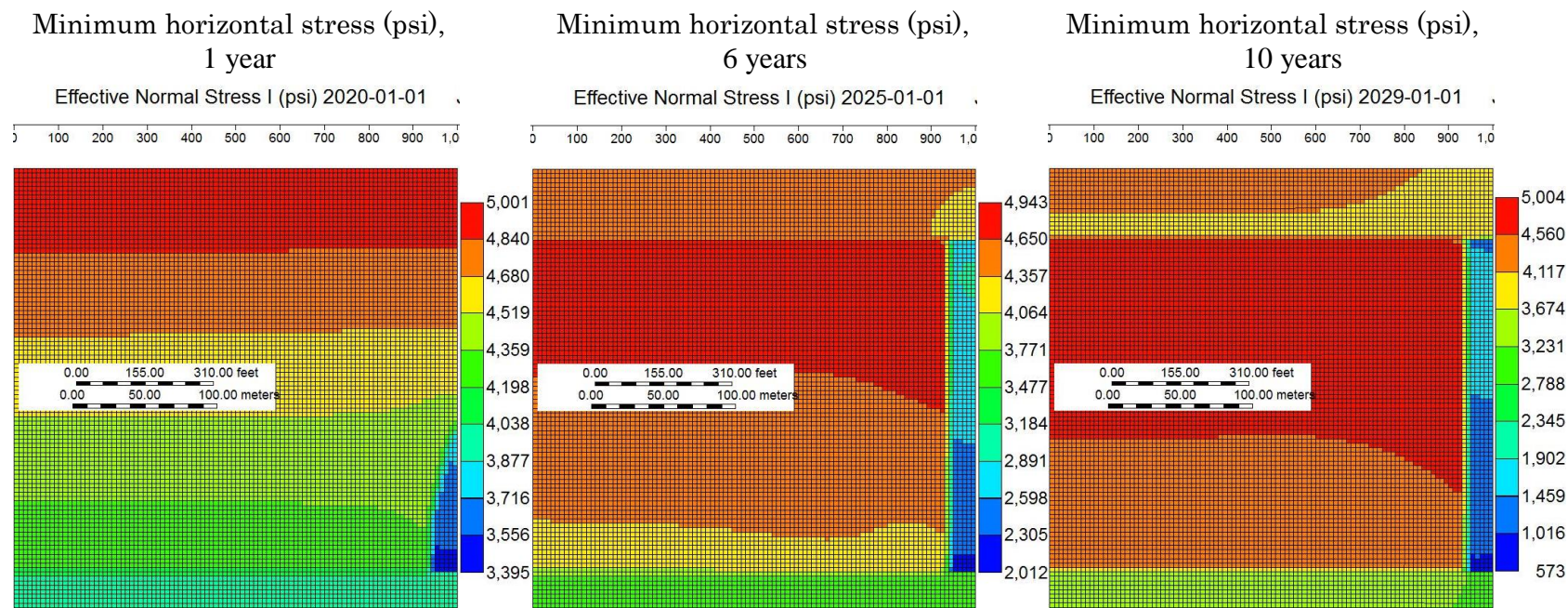
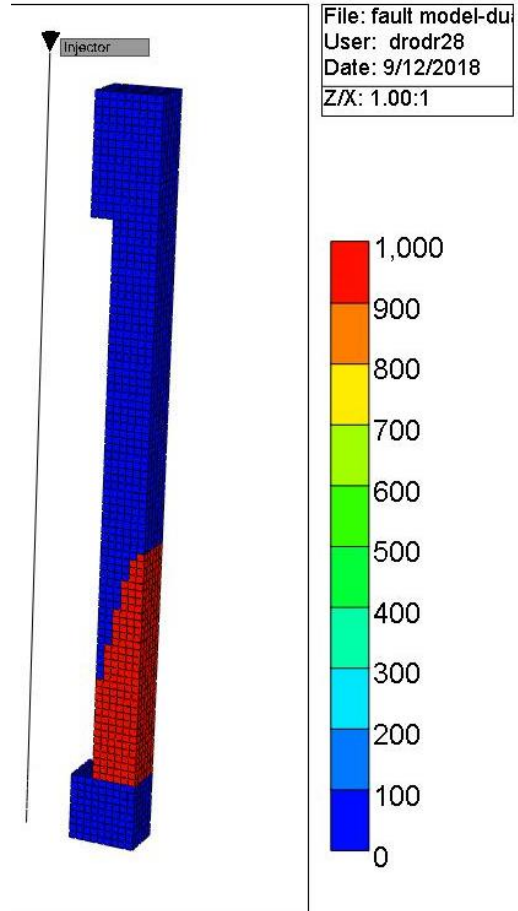


Figure 6.5. Minimum horizontal stress in the matrix for the dual-permeability fault model with simple geometry. Minimum horizontal stresses decrease in the damage zone and the sandstones as a consequence of injection-induced overpressures.



Fracture permeability profile (md), 1 year



Fracture permeability profile (md), 10 years

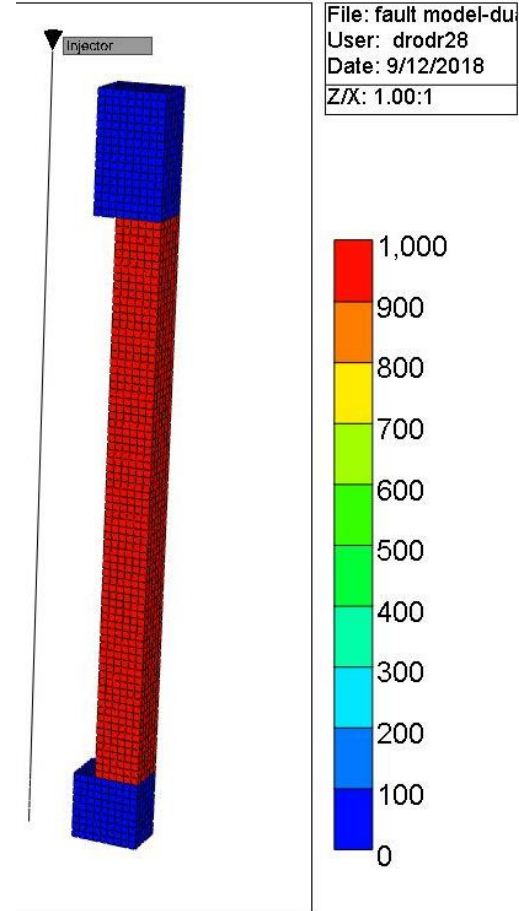


Figure 6.6. Vertical fracture permeability changes due to Geomechanics. Contour graphs of the damage zone for the dual-permeability fault model with simple geometry. After ten years of simulation, all the fractures in the shale have permeabilities in the range of 900 to 1000 md.

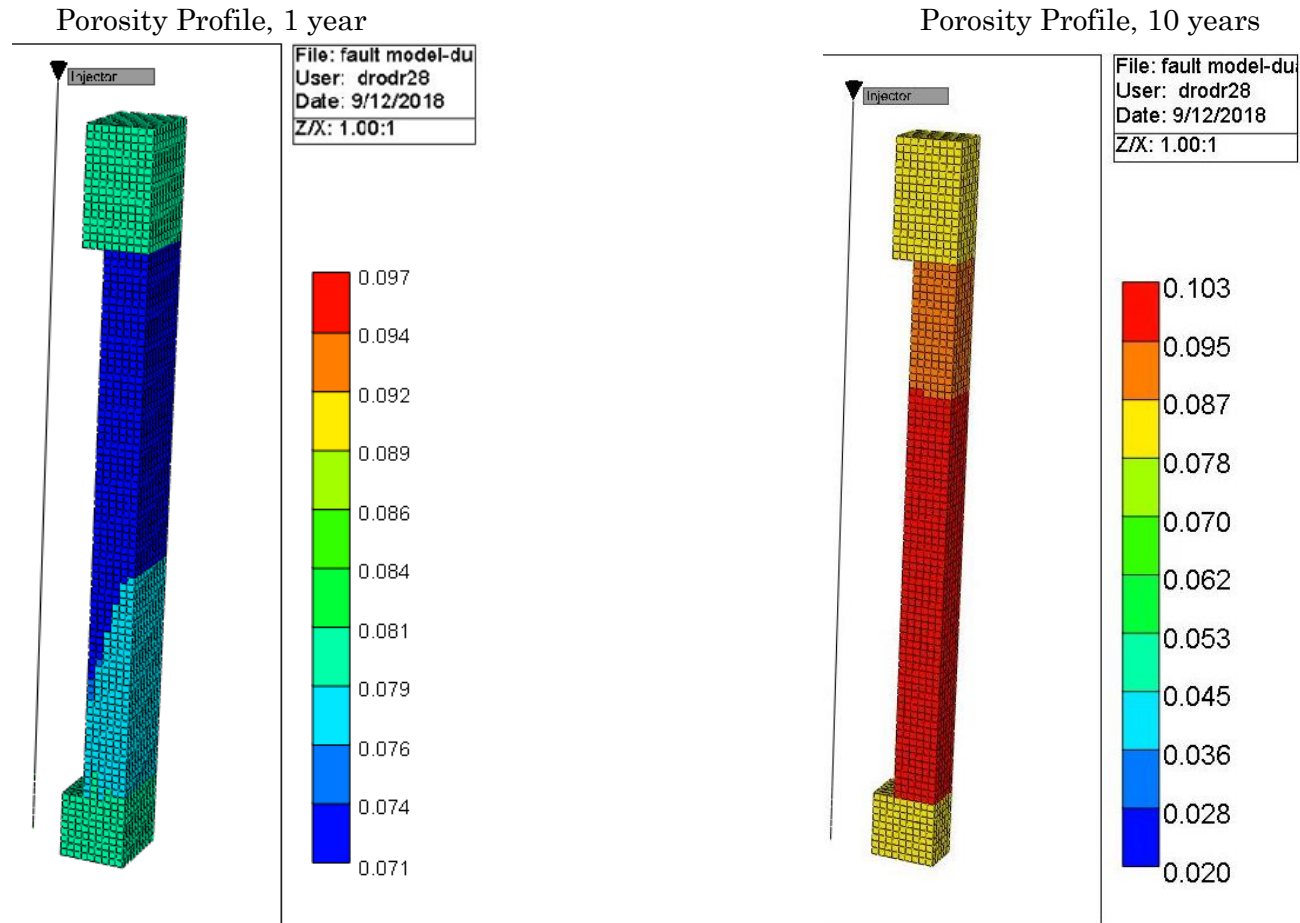


Figure 6.7. Porosity changes due to Geomechanics– Matrix. Contour graphs of the damage zone for the dual-permeability fault model with simple geometry. Porosity in the shale increases from 8% to an average of 9.5% after ten years of injection.

In the following we investigate the pressure/stress behavior at different locations along the CO<sub>2</sub> migration path. The locations of interest are shown in Figure 6.8 and are listed explicitly below.

1. 850 ft from the core of the fault in the upper sand and 90 ft from the top of the domain.
2. 30 ft from the core of the fault in the damage zone of the upper sand, and 160 ft from the top of the domain.
3. 850 ft from the core of the fault in the lower sand, and 960 ft from the top of the domain.
4. 30 ft from the core of the fault in the damage zone of the upper sand, and 910 ft from the top of domain.
5. 560 ft from the core of the fault in the shale, and 520 ft from the top of the domain.
6. 60 ft from the core of the fault in the shale, and 510 ft from the top of the domain.
7. 30 ft from the core of the fault in the damage zone of the shale and 170 ft from the top of the domain.



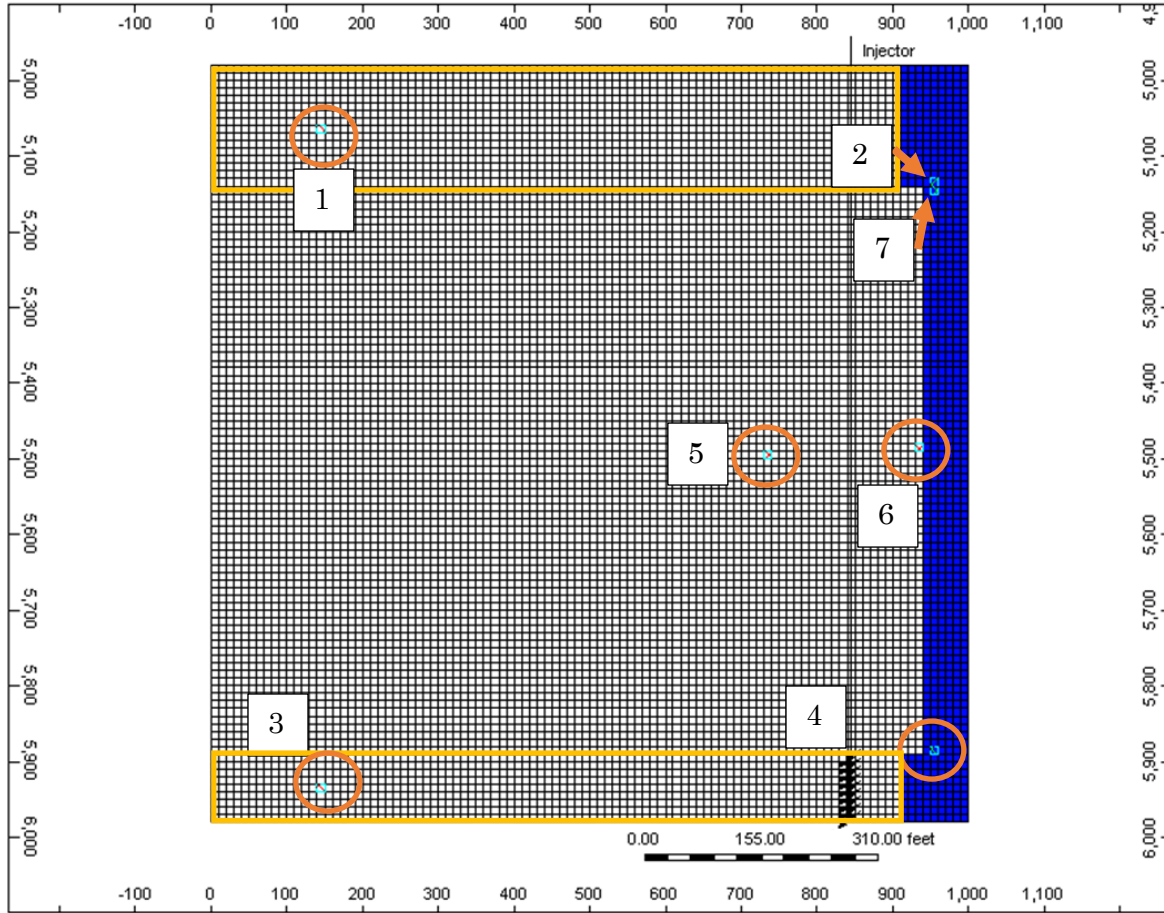


Figure 6.8. Location of the seven blocks used to study permeability, pressure and normal effective stresses during ten years of CO<sub>2</sub> injection.

Due to the proximity of the injection well to the damage zone and given the injection rate and flow capacity of the sandstone, there is relatively fast CO<sub>2</sub> migration in the lower sand. Figure 6.9 demonstrates that the normal effective stress changes non-monotonically at the lower portion of the damage zone of the shale (location 4). The early drop of the effective stress is simply due to the increase in the pressure. However, the pore pressure plateaus as more of the fractures open up inside the damage zone, allowing the injected fluid to dissipate. The increment of stress observed after the pressure plateau is caused by the breakthrough of brine from the shale into the upper sand. Since the damage zone in the sand has a higher permeability than that in the shale, brine influx causes a reduction of pressure and an increase of stress. After the fractures are opened throughout

the damage zone the pressure continuously increases while the injection continues, causing the stress to drop. The dormant fractures in the shale begin to open after 149 days of injection when the normal fracture effective stress in the block reaches a value of approximately 3812 psi. Once the fractures open, their permeabilities can reach a maximum of 1,000 md. As a result, CO<sub>2</sub> flows upwards through the damage zone fractures toward the upper zone (location 7 at the top of the shale damage zone). CO<sub>2</sub> reaches location 3, about 800 feet from the injection site in the lower sandstone, after 609 days of injection when the normal fracture effective stress is around 4492 psi, at which fracture permeability also reaches 1,000 md as specified for the Barton-Bandis input parameters.

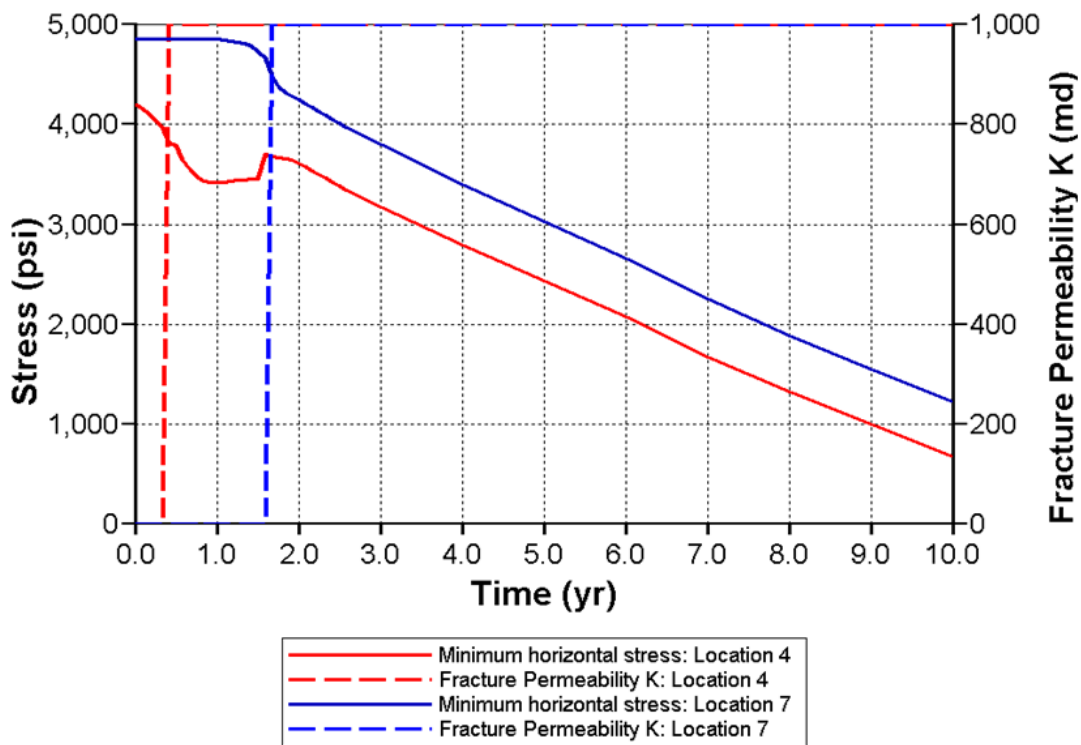


Figure 6.9. Normal effective stresses and permeability changes for blocks 4 and 7 throughout the injection period. Fractures at the bottom of the shale (Location 4) open after 149 days (0.4 years). Dormant fractures at the top of the shale (Location 7) are activated after 609 days (1.7 years).

Figure 6.10 includes several stress profiles for locations 1 to 6. It can be observed that minimum horizontal stresses in location 1 experiences a reduction of 830 psi, and location 2 shows a reduction of 1210 psi after ten years of injection. Minimum horizontal stresses decrease by 880 psi in location 3, and by 3,530 psi in location 4 at the end of the injection period. For location 5 situated in the middle of the shale but far from the damage zone it is evident that pore pressure does not change because brine nor CO<sub>2</sub> pressure is enough to allow fluid entrance into the shale host rock because of its very low permeability (0.1 nd). However, minimum horizontal stress shows a decrement of 20 psi at the end of the injection period as a result of deformation in the damage zone. In location 6, however, there are stress changes that may be caused by both deformations in the damage zone and brine or CO<sub>2</sub> flow. Minimum horizontal stress in location 6 shows a reduction of 625 psi after 10 years.

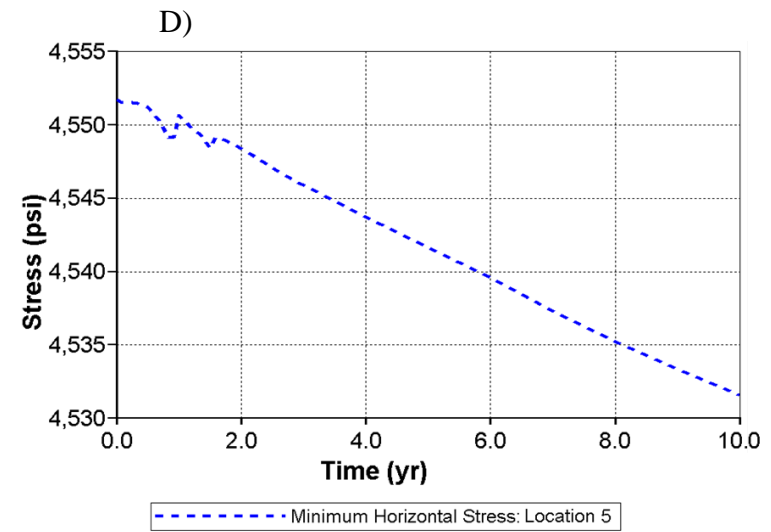
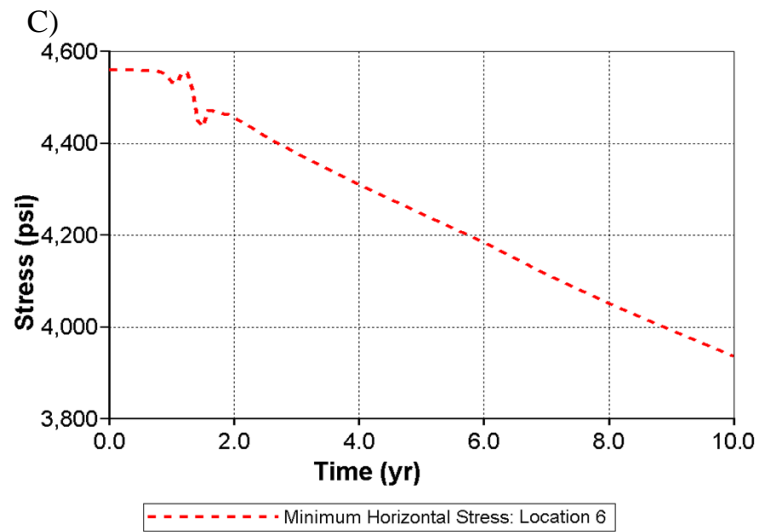
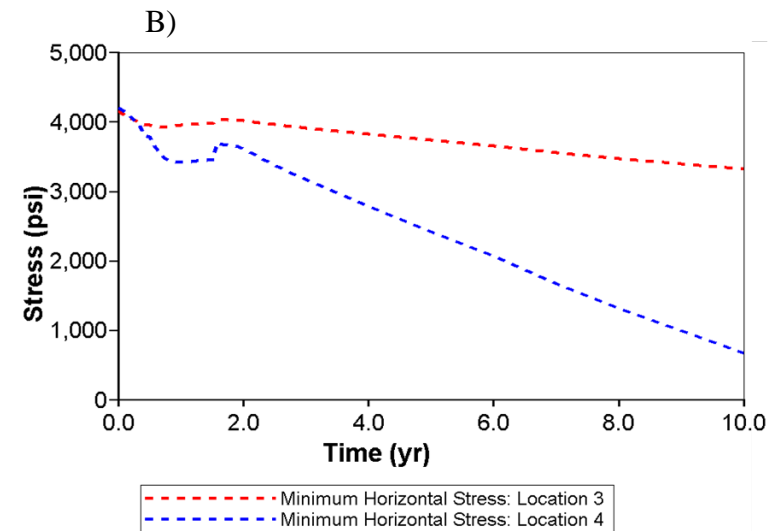
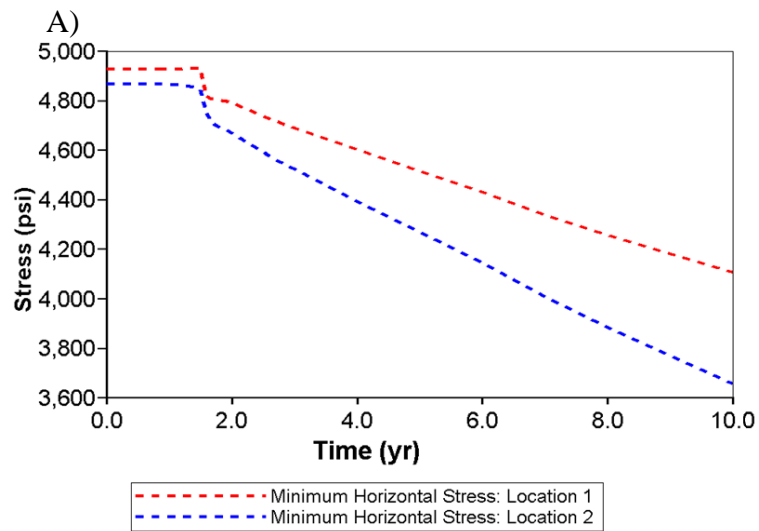


Figure 6.10. Figures A to D represent minimum horizontal stress changes for locations 1, 2, 3, 4, 5 and 6.

## Chapter 7. Coupled Modeling of a Geologically Realistic Fault Effect on CO<sub>2</sub> Storage Integrity

In departure from the idealized fault structure modeled in the previous chapter, we present a more realistic fault which may represent faults present in potential CO<sub>2</sub> storage sites in Louisiana (Zulqarnain et al., 2017). Like the previous chapter, the model includes a dual permeability approach to account for fractures in the damage zone. Initially, the fractures in the damage zone are dormant; fractures could allow the fluid to pass along the damage zone only if they are activated due to geomechanical forces.

### 7.1. Model Description

The model is similar to the one in Chapter 6 in the sense that it comprises two sandstone layers and a shale formation lying in the middle of the sandstones. The lateral sealing fault has an impermeable core and a damage zone with different geometrical and petrophysical characteristics in the sandstones and the shale. The damage zone contains fractures that are not active at the beginning of injection. Mechanical properties of the sands and the shale are presented in Table 7.1.

The properties were applied to the damage zone and the host rock.

Table 7.1. Mechanical properties used for the simulation and study of a realistic model (Molina et al., 2017; Rutqvist et al., 2013).

| Parameters                 | Shale | Upper and lower sand |
|----------------------------|-------|----------------------|
| Young's modulus, E (psi)   | 4.3E6 | 2.9E6                |
| Poisson's ratio, $\nu$ (-) | 0.25  | 0.2                  |
| Joint cohesion (psi)       | 870   | 100,000              |

The model is representative of a 780 ft thick shale formation that is bounded at the top by a 130 ft thick sandstone and at the bottom by a 270 ft sand formation in north Louisiana. The same hydraulic and mechanical properties are used for both sandstones. This 3-layer system is intersected by a normal fault with a dip angle of 70° and an initial offset displacement of 155 ft.

Fractures in the damage zone are equally distributed with a constant fracture spacing of 5 ft in the sands and 10 ft in the shale. The damage zone in the upper and lower sands has a thickness of 68 ft measured perpendicular to the fault plane. The thickness of the damage zone in the shale has an average thickness of 57 ft also measured perpendicular to the fault plane (See Figure 7.1).

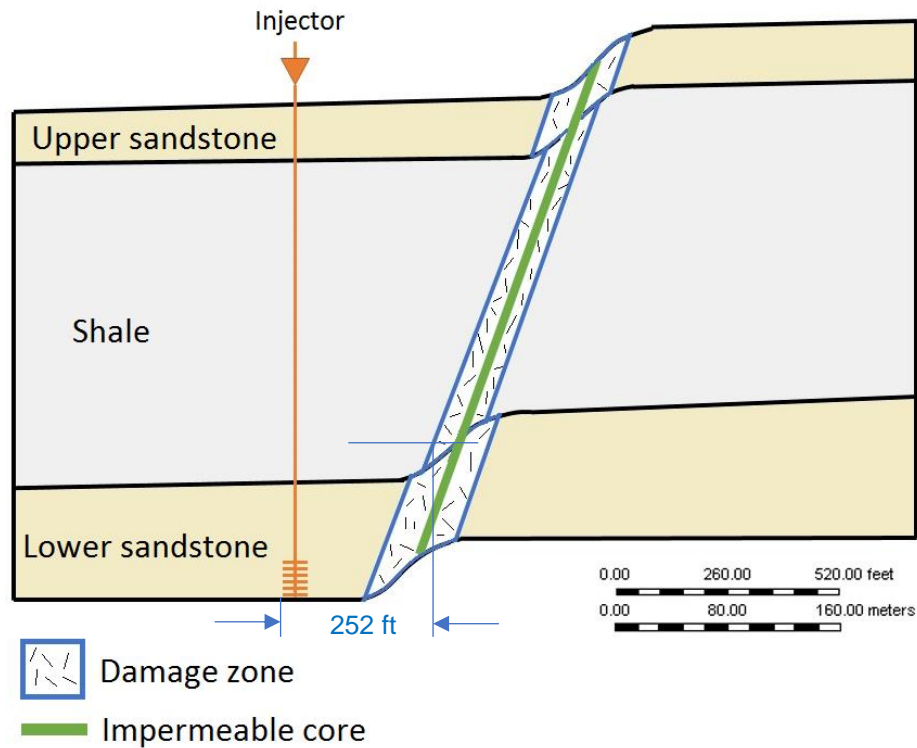


Figure 7.1. Cross-sectional configuration used for the realistic simulation. The model resembles a CO<sub>2</sub> storage site in Louisiana (Zulqarnain et al., 2018)

The initial pore pressure gradient is 0.465 psi/ft, and the thermal gradient is 8.54 °F/1000 ft.

In this study, the stress field is typical of a normal fault where the vertical stress ( $\sigma_v$ ) is the maximum compressive stress, and the minimum compressive stress is the minimum horizontal stress ( $\sigma_h$ ). Therefore,  $\sigma_v > \sigma_H > \sigma_h$ , where  $\sigma_H$  signifies the maximum horizontal stress. We set the maximum principal stress gradient (vertical stress) to 1.17 psi/ft corresponding to a gradient of 168.6 lb/ft<sup>3</sup> density of overburden (Cipolla et al., 2010; Rutqvist et al., 2013; Starr, 2011). The minimum compressive stress gradient was set to 0.7 psi/ft.

Shale formations generally tend to be brittle (Rutqvist et al., 2013). For a rock with a composition of 25% clay and a Poisson's ratio of 0.25, the Young's modulus is 4.3E6 psi (equivalent to 30 GPa) (Guo et al., 2012). The cohesion for the shale is set to 870 psi (6 MPa). Sand is less friable with a Young's modulus of 7.25E5 psi (5 MPa) and a Poisson's ratio of 0.2 (Molina et al., 2017). For the simulation the cohesive strength of the sandstone is set to 100,000 psi.

The permeability of the damage zone of the fractures is a crucial parameter for the simulation. The vertical permeabilities are one tenth of the horizontal permeabilities. The matrix and fractures in the damage zone located in the shale are assumed to have very low conductivity with a horizontal permeability of 100 nd and vertical permeability of 10 nd. Similar permeability values are found in real shale formations such as the Opalinus shale in Switzerland where both the matrix and the damage zone are hydraulically undistinguishable having a permeability of 20 nd despite the fact that the damage zone is highly fractured, meaning that the fractures are practically closed (Croisé et al., 2004; Rutqvist et al., 2013). Input data for permeability in the damage zones and host rocks are displayed in Table 7.2.

Table 7.2. Permeability table for the matrix and fractures for the system in the realistic simulation model (Croisé et al., 2004; Rutqvist et al., 2013).

|                                  |           | Host rock                             |                                     | Damage zone                           |                                     |
|----------------------------------|-----------|---------------------------------------|-------------------------------------|---------------------------------------|-------------------------------------|
|                                  |           | Horizontal permeability<br>$k_h$ (md) | Vertical permeability<br>$k_v$ (md) | Horizontal permeability<br>$k_h$ (md) | Vertical permeability<br>$k_v$ (md) |
| <b>Upper and lower sandstone</b> | Matrix    | 600                                   | 60                                  | 6                                     | 0.6                                 |
|                                  | Fractures | -                                     | -                                   | 0.1                                   | 0.01                                |
| <b>Shale</b>                     | Matrix    | 2E-5                                  | 2E-6                                | 0.0001                                | 1E-5                                |
|                                  | Fractures | -                                     | -                                   | 0.0001                                | 1E-5                                |

When fractures that were once closed are activated, a change in fracture width occurs along with permeability and porosity changes. This fracture aperture is usually between 100 and 200  $\mu\text{m}$ .

With this change of fracture aperture permeability increases by 3 to 5 orders of magnitude (Rutqvist et al. (2013)). For the present study, the maximum permeability after activating the dormant fractures is set to 10 md. Table 7.3 provides the necessary input parameters for the Barton-Bandis model.

Table 7.3. Variables used for calculation of permeability after fractures activation with the Barton-Bandis model in the realistic model setup (Ketzer et al., 2012; Rutqvist et al., 2013).

|   |           |
|---|-----------|
| <b>Initial fracture aperture, <math>E_0</math> (Ketzer et al.)</b>                | 6.5E-5    |
| <b>Initial normal fracture stiffness, <math>k_{ni}</math> (psi/ft)</b>            | 3.2284E-6 |
| <b>Fracture opening stress (psi)</b>  | -300      |
| <b>Hydraulic fracture permeability, <math>f_{rs}</math> (md)</b>                  | 10        |
| <b>Fracture closure permeability, <math>k_{ccf}</math> (md)</b>                   | 10        |
| <b>Residual value of fracture closure permeability, <math>k_{rcf}</math> (md)</b> | 1         |

The relative permeability curves used for the realistic model were also obtained from Krevor et al. (2012) and they are the same used for the simple geometry model (Figure 6.2).

## 7.2. Simulation results

The simulation results are obtained for a constant CO<sub>2</sub> injection rate of 500,000 ft<sup>3</sup>/day for 30 years. The perforated interval for injection is located at the lowermost 500 ft. The well is vertical and is located 252 ft from the core of the fault, distance measured at the top of the lower sandstone.

Due to the geomechanical opening of the fractures, CO<sub>2</sub> starts leaking through the bottom of the shale after approximately six years of injection. The CO<sub>2</sub> mole fraction is still meager and therefore not graphically represented in Figure 7.3. However, CO<sub>2</sub> flow in the damage zone does not accompany fracture initiation. The first opened fractures in the shale's damage zone occur after 180 days of injection due to a pressure buildup of the brine in the lower sandstone. Fracture openings in the damage zone of the upper sand start occurring at the 25<sup>th</sup> year of injection, while CO<sub>2</sub> starts breaking in after 27 years of injection.



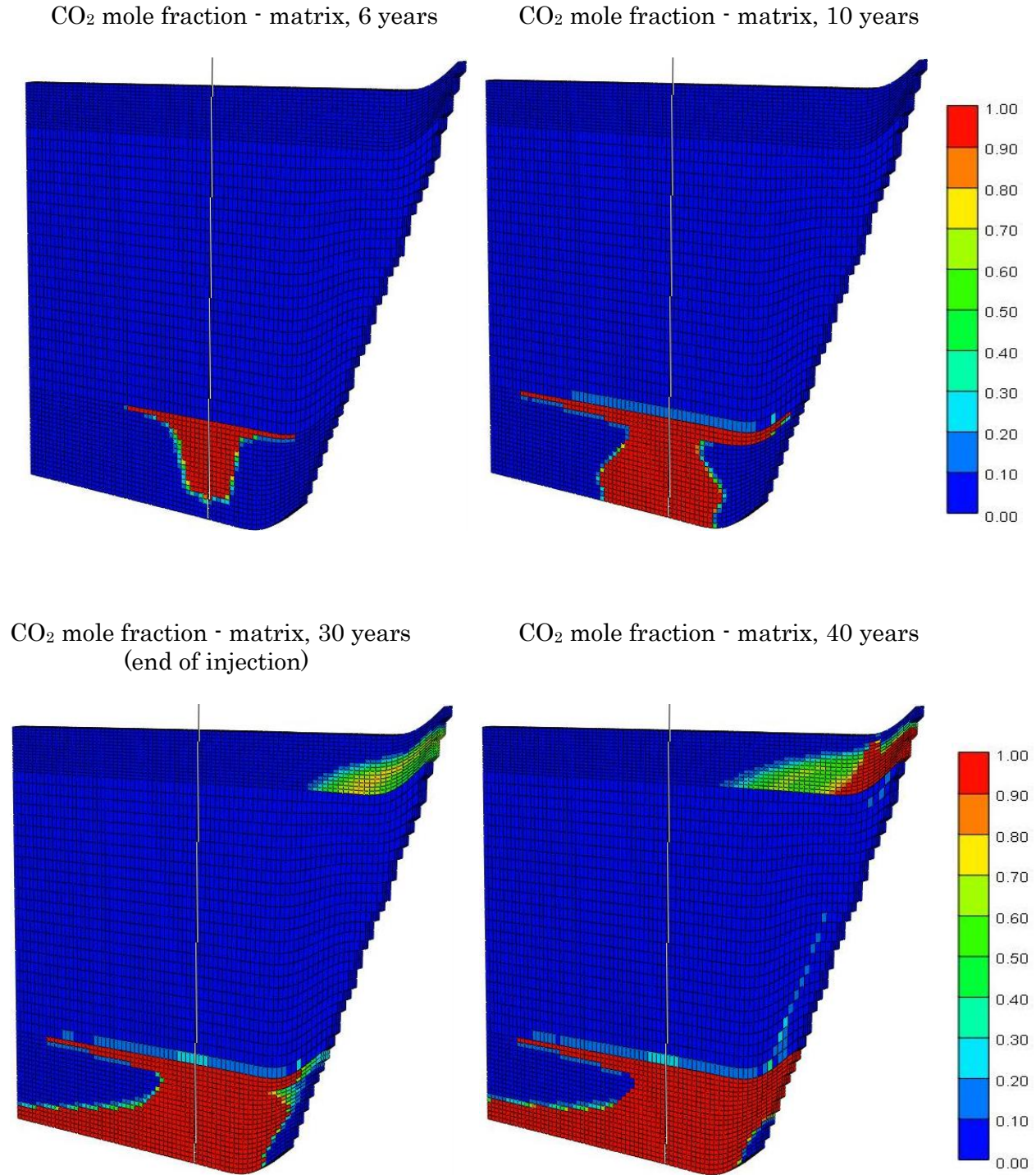


Figure 7.2. Contour maps of CO<sub>2</sub> mole fraction distribution in the matrix for the dual-permeability model with real geometry at different times during the injection period (after 10, 20 and 30 years) and post-injection (after 40 years of simulation).

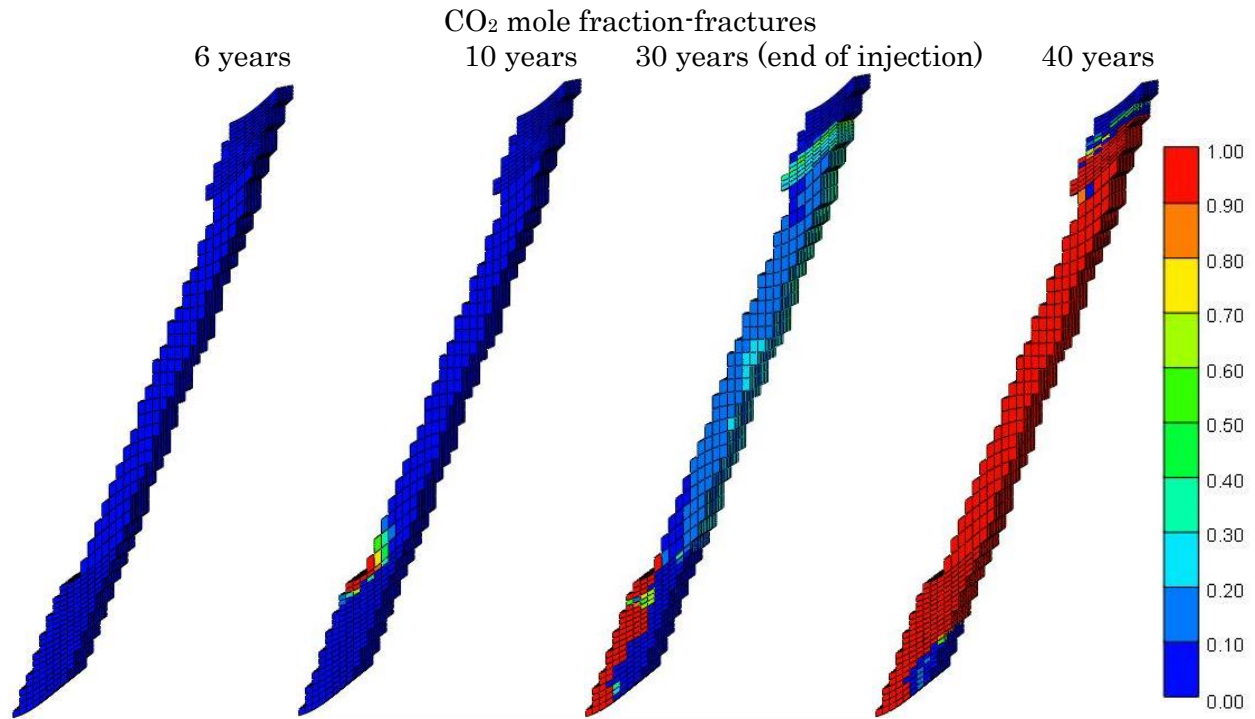


Figure 7.3. CO<sub>2</sub> mole fraction in the fractures of the damage zone for the model with realistic geometry at different times during the injection period (after 10, 20 and 30 years) and post-injection (after 40 years of simulation).

Figures 7.2 and 7.3 present the CO<sub>2</sub> mole fraction in the matrix and the fractures at different times during and after the injection period. As in the simple geometry model of the previous chapter (see Figure 7.2), the main pathway for the CO<sub>2</sub> plume from the lower to the upper sand is through the fractures in the damage zone.

An important observation in Figures 7.2 and 7.3 is that even 10 years after the injection well is shut-in, CO<sub>2</sub> continues flowing along the fault and towards the upper sand. Reasons for this behavior include gravitational segregation where the CO<sub>2</sub> moves upwards due to its lighter density and continued overpressurization in the injection zone providing a driving force for continued leakage. The pressure dissipates over time leading to the closure of fractures in the damage zone when the pressures fall below the closure pressure.



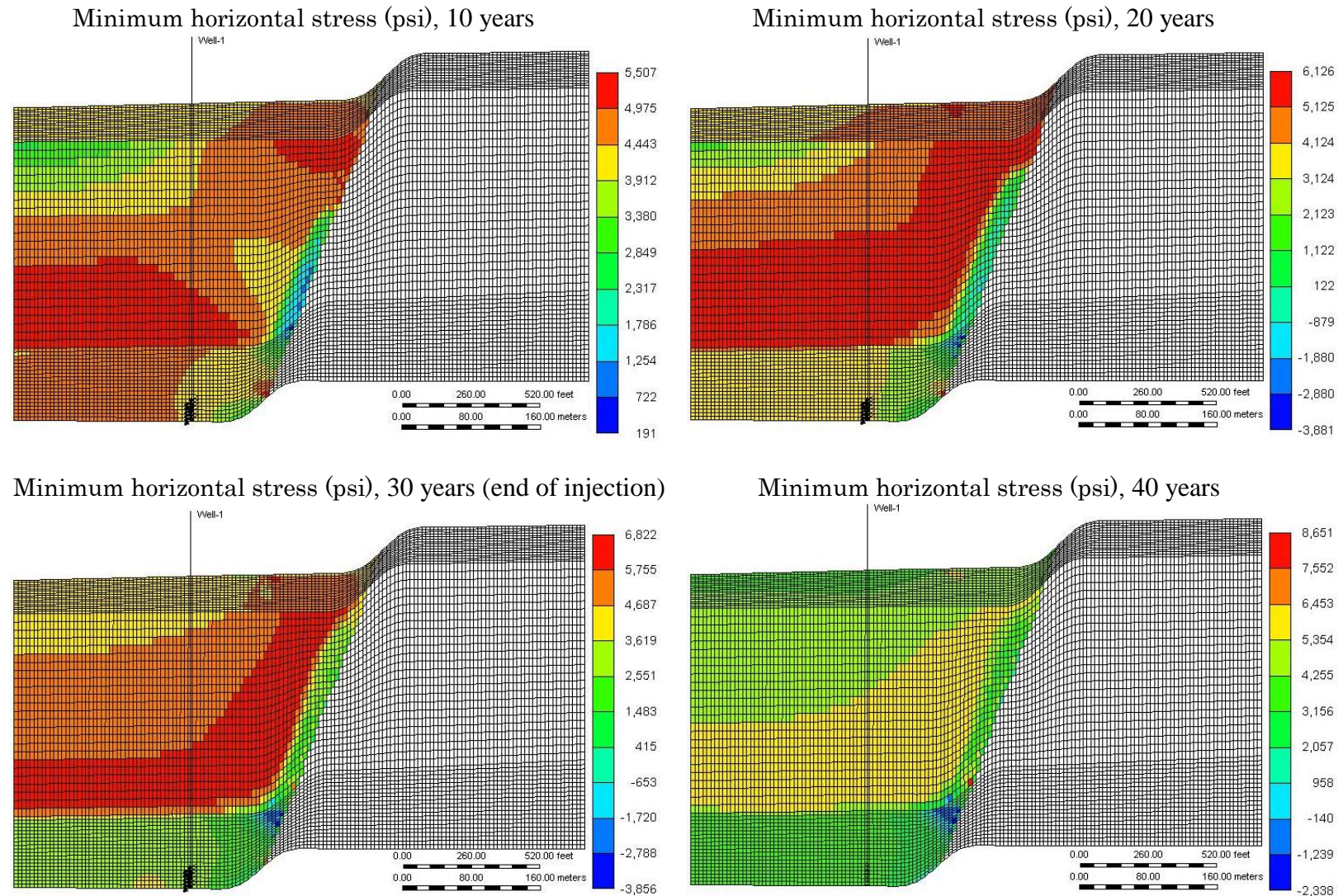


Figure 7.4. Minimum horizontal stress contour graphs for the realistic model at different times during the injection period (after 10, 20 and 30 years) and post-injection (on 2059 and after 40 years of simulation).

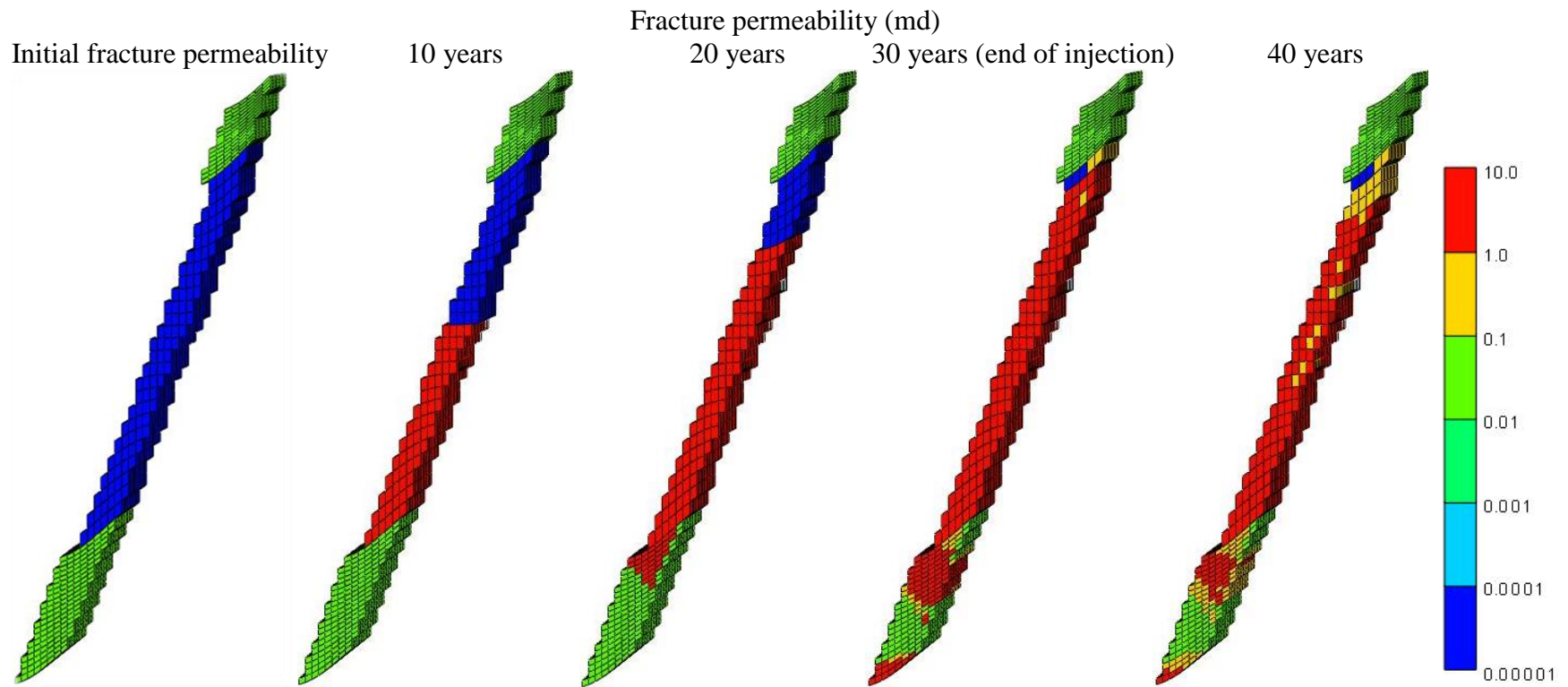


Figure 7.5. Evolution of vertical fracture permeability in the damage zone at different times of CO<sub>2</sub> injection and after ten years of injection ceases.

The effective minimum horizontal stress is shown in Figure 7.4. As observed, the average minimum horizontal stress in the lower sand reduces by about 2500 psi at the end of the 30 years of injection. The stress in the damage zone of the shale decreases by an average of 600 psi after the injection period due to the increasing pore pressures caused by CO<sub>2</sub> injection.

The vertical permeabilities evolution in the fractures is shown in Figure 7.5. Ten years after injection ceases (or 40 years of simulation), fracture vertical permeabilities in several grid blocks reduce to values between 0.1 and 1 md. This phenomenon is observed because, in the absence of injection, the normal effective stress increases until surpassing its threshold value. When this happens, fracture apertures start closing, which translates to a permeability reduction. However, permeabilities do not reach initial values due to the plasticity of the rock.

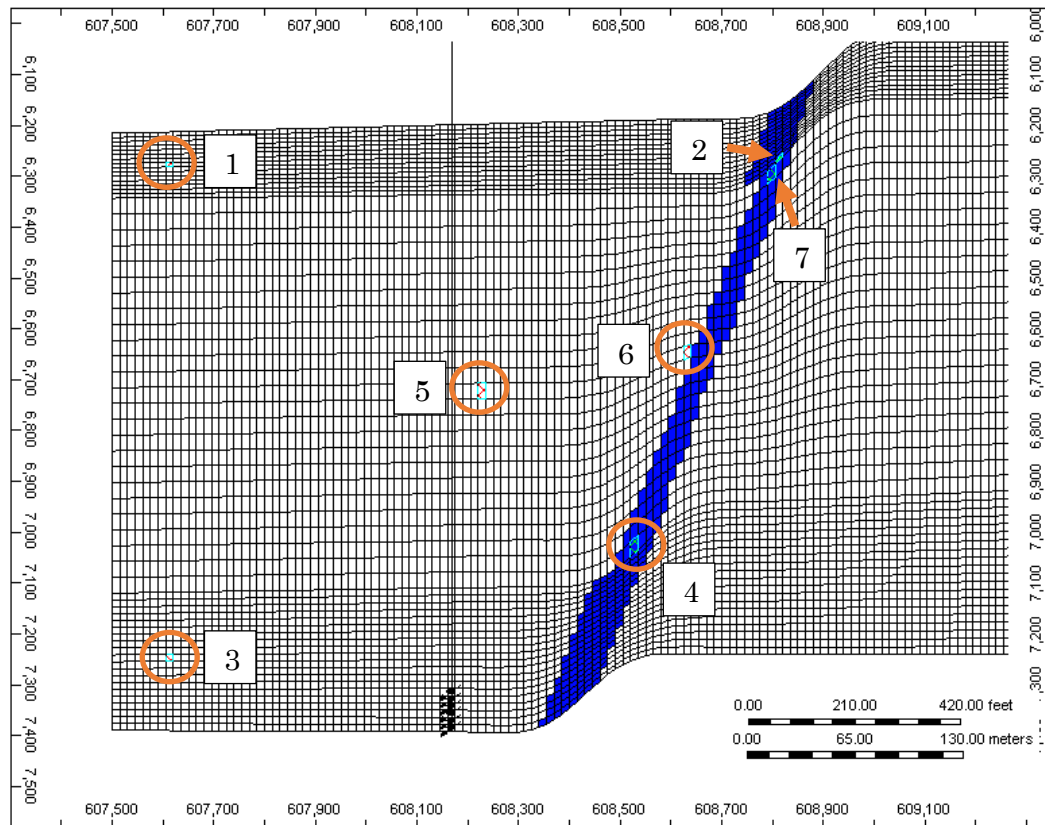


Figure 7.6. Location of the 7 blocks used for the analysis of permeability, pressure and minimum effective stress.

Similar to Chapter 6, we present the leakage pressure behavior at several locations of interest. The locations of interest are shown in Figure 7.5 and are listed in detail below.

1. 1250 ft from the core of the fault in the upper sand and 80 ft from the top of the upper sandstone.
2. 20 ft from the core of the fault in the damage zone of the upper sand, and 100 ft from the top of the upper sandstone.
3. 880 ft from the core of the fault in the lower sand and 120 ft from the top of the lower sandstone.
4. 50 ft from the core of the fault in the damage zone of the lower sand, and 220 ft from the base of the lower sandstone.
5. 470 ft from the core of the fault in the shale, and 530 ft from the top of the upper sandstone.
6. 60 ft from the core of the fault in the shale, and 450 ft from the top of the upper sandstone.
7. 30 ft from the core of the fault in the damage zone of the shale and 70 ft from the top of the upper sandstone.

For locations 3 and 4 (both in the lower sandstone) pressure increases due to CO<sub>2</sub> injection for approximately 27 years. After this period, pore pressure declines because the CO<sub>2</sub> plume reaches the upper sand and pressure is then dissipated in the lower sand. When injection stops after 30 years, the CO<sub>2</sub> plume continues flowing towards the upper sand, resulting in an additional pressure reduction in the lower sand for ~1.5 years. When all the pressure dissipates, and under the absence of injection, the pore pressure remains almost constant until the end of the simulation, which is ten years after the end of injection. Minimum horizontal stresses reduce at different rates until 27 years of injection. In location 4 (near the base of the caprock damage zone) there is a marked change in stress at the 9<sup>th</sup> year of injection that may arise from a significant fracture permeability change in



the base of the shale. The stress remains almost constant from the 21<sup>st</sup> to the 27<sup>th</sup> year of injection as more fractures open in the damage zone. When the CO<sub>2</sub> breaks through at the upper sand, the minimum horizontal stress increases as a result of pore pressure reduction. After the injection well is shut in, the stress will continue increasing for about 1.5 years due to the contained overpressure after the injection. After this period, stress will remain more or less constant until the end of the simulation (Figure 7.7).

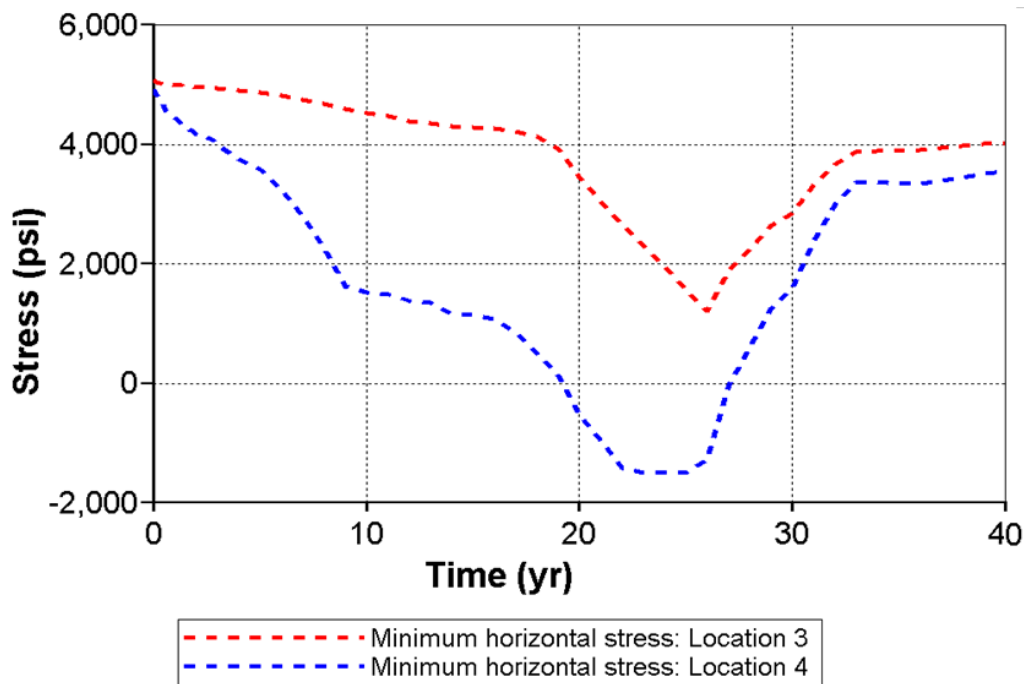


Figure 7.7. Minimum horizontal stress and pore pressure profiles for locations 3 and 4, both located in the lower sand. The profiles show results for the 30 first years of injection and ten more years of post-injection.

For the locations of study in the upper sand, we can observe that pore pressure will remain constant until fluids start to enter the formation after 26 to 27 years of injection. At that period of time, the pressure in location 2 (at the top of the caprock damage zone) rises considerably until 1.5 years after injection. The pressure in location 1 (located far from the fault in the upper sandstone) increments more slowly than that in location 2. Stresses in locations 1 and 2 continue increasing

for a short period after the injector well is closed. After the 32<sup>nd</sup> year of simulation the pressure in location 1 continues increasing with a lower slope.

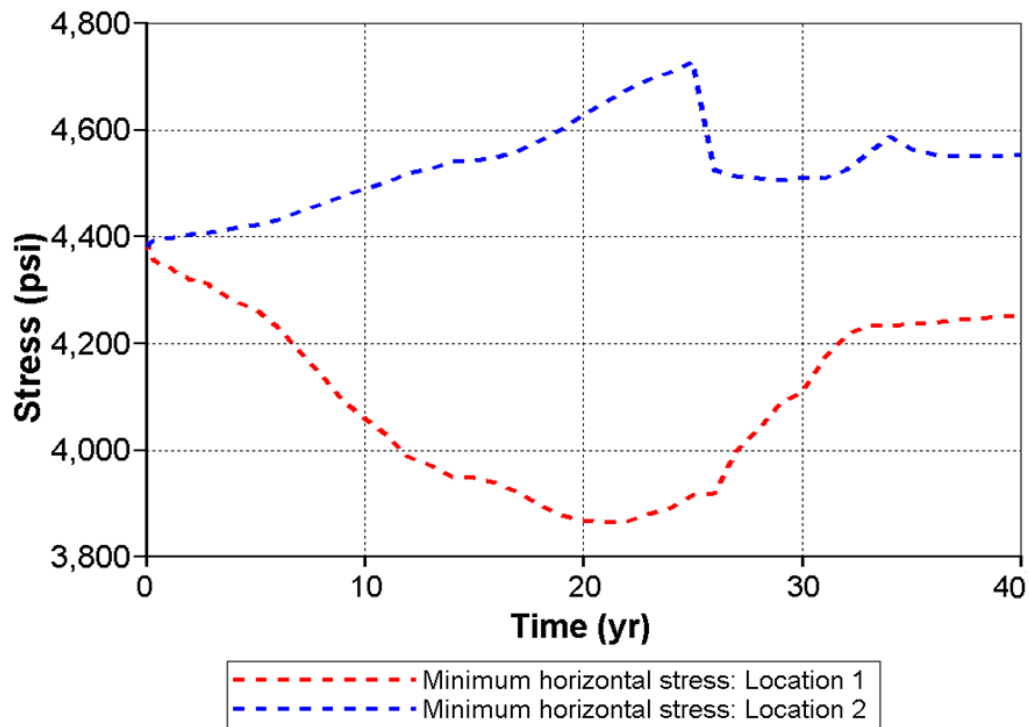


Figure 7.8. Minimum horizontal stress and pore pressure profiles for blocks 1 and 2, both located in the lower sand. The profiles show results for the 30 first years of injection and ten more years of post-injection.

For location 5, which is in the middle of the shale but far from the damage zone of the fault, pore pressure remains constant throughout the injection and post-injection periods. Minimum horizontal stress shows a reduction in the first 10 years of injection and an increase for the next 17 years where the stress starts decreasing due to the intrusion of fluids in the upper sandstone (Figure 7.9).



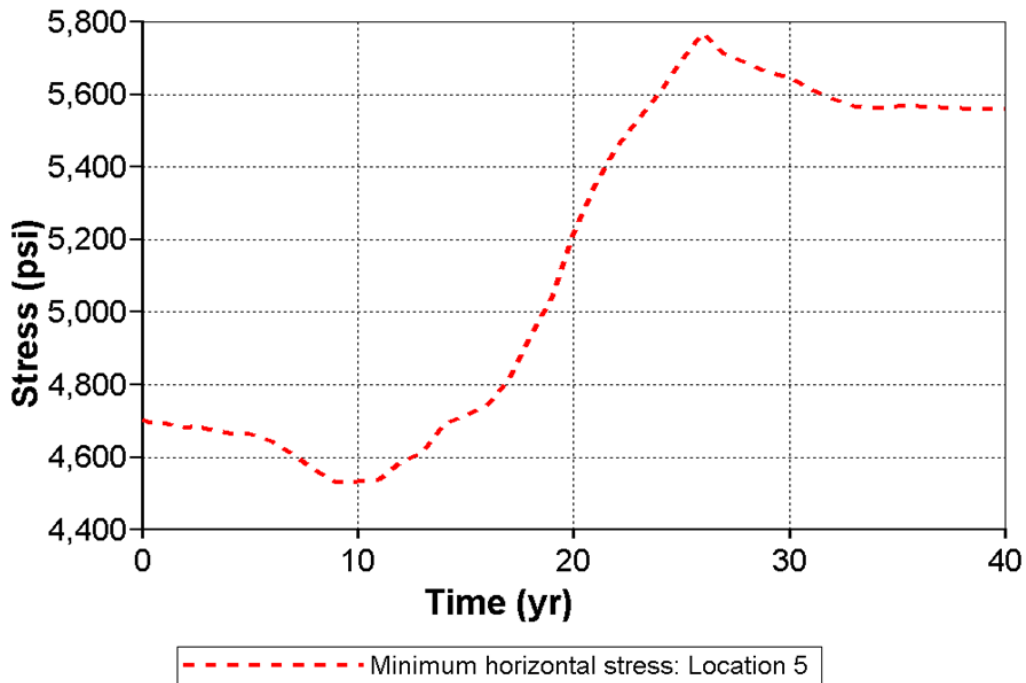


Figure 7.9. Minimum horizontal stress and pore pressure profiles in the middle of the caprock (location 5). The profiles show results for the 30 first years of injection and ten more years of post-injection.

In the shale pores neighboring the damage zone in the middle of the confining unit (location 6) there are pressure and stress changes that may be caused purely by geomechanical forces or due to brine displacement that occurs due to the proximity to the damage zone. The pressure remains constant until the 8<sup>th</sup> year of injection, and it increases until the fluid breaks in the upper sandstone after 25 years of injection, then it starts decreasing until the 34<sup>th</sup> year of simulation. Finally, for the last 6 years of post-injection, pressure increases slightly and then remains almost constant. The minimum horizontal stress increases slightly after the first eight years of injection, then reduces 3617 psi until the 25<sup>th</sup> year of injection, but when there's breakthrough of fluids in the upper sandstone, the stress starts increasing until the 34<sup>th</sup> year. After this year the stress has some minor variations (Figure 7.10).

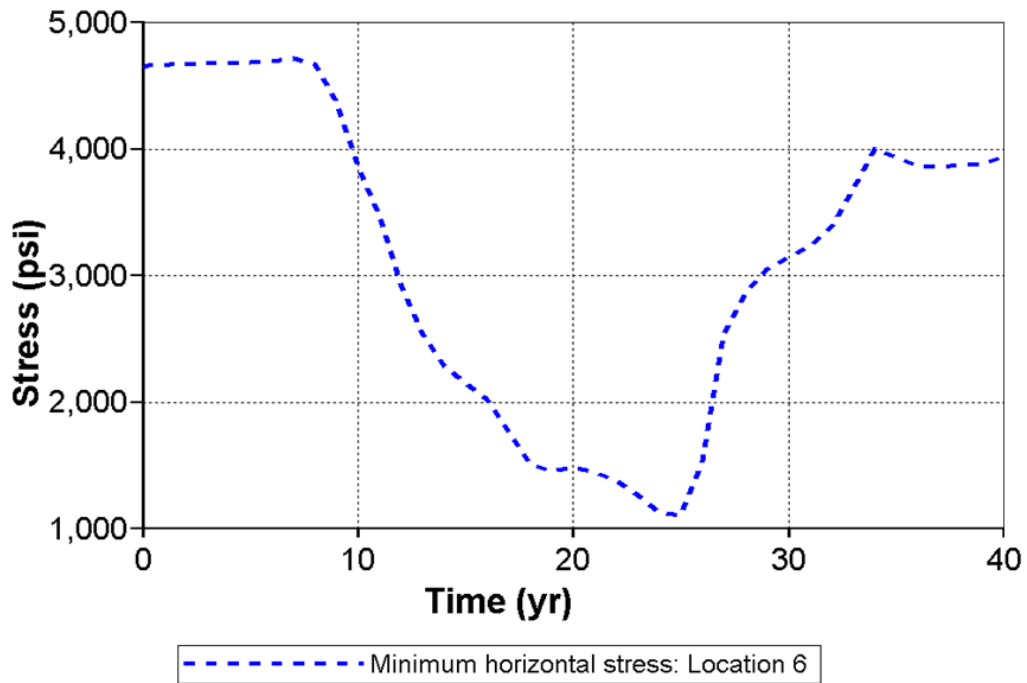


Figure 7.10. Minimum horizontal stress and pore pressure profiles for location 6 (in the caprock and contiguous to the damage zone). The profiles show results for the 30 first years of injection and ten more years of post-injection.

## Chapter 8. Conclusions

In this work, three different simulation cases were conducted by using CMG-GEM (2017) to investigate the effect of a fault on the storage of CO<sub>2</sub> in underground saline aquifers. This study can be concluded with three major conclusions as follows.

- This study numerically shows the importance of poro-elastic/plastic behavior of fault zone and hysteresis in fracture permeability change for realistic modeling of flow through fault zone in CO<sub>2</sub> sequestration applications. When CO<sub>2</sub> is injected near a fault zone, injection pressure causes the fractures in the damage zone to be geomechanically activated. The fractures in the damage zone then have a higher permeability forming conductive pathways for CO<sub>2</sub> migration.
- When an ideal model with multiple horizontal layers and a vertical lateral sealing fault is investigated, three major observations can be reported from the simulation results. First, the breakthrough of CO<sub>2</sub> into the lower sand occurs after 120 days of injection and into the upper sand after 1.7 years of injection. Second, the fractures permeability in the damage zone in the caprock reaches a maximum hydraulic permeability of 1000 md. Third, the porosity in the damaged zone increases from 8% to values in the range of 8.7 to 10.3%.
- When a model based on a tilted lateral sealing fault located in a potential site of CO<sub>2</sub> storage in Louisiana is studied, the three major observations are summarized as follows. First, the times of fracture activation and CO<sub>2</sub> breakthrough are not the same; in fact the fractures are open long before CO<sub>2</sub> reaches these fractures. Second, permeability of most fractures in the shale's damage zone reach the hydraulic permeability of 10 md after the injection period ends. After 10 years of post-injection several regions experience a reduction in permeability to values higher than the residual permeability following the Barton-Bandis

model. Third, the porosity in the shale's damage zone increases from 1% to values in the range of 1.11 to 1.59% at the end of injection.

This work did not account for heterogeneities in the damage zone, capillary pressure effects, or geochemical reactions. Future research work may include these processes for more detailed and accurate simulations results.

## References

- N. E. T. L. (2015). Carbon Storage Atlas. In *Carbon Storage Atlas* (5th Edition ed.): U.S. Department of Energy.
- Anders, M. H., & Wiltschko, D. (1994). Microfracturing, paleostress and the growth of faults. *16*(6), 795-815.
- Bandis, S. C., Lumsden, A. C., & Barton, N. R. (1983). Fundamentals of rock joint deformation. *International Journal of Rock Mechanics and Mining Sciences & Geomechanics Abstracts*, *20*(6).
- Blenkinsop, T. G. (2007). *Deformation microstructures and mechanisms in minerals and rocks*: Springer Science & Business Media.
- Blunt, M. (2010). Carbon dioxide storage. 4.
- Britannica, T. E. o. E. (2018). Fault | geology. *Encyclopædia Britannica*. Retrieved from Encyclopædia Britannica website: <https://www.britannica.com/science/fault-geology>
- Childs, C., Manzocchi, T., Walsh, J. J., Bonson, C. G., Nicol, A., & Schöpfer, M. P. J. J. o. S. G. (2009). A geometric model of fault zone and fault rock thickness variations. *31*(2), 117-127.
- Cilona, A., Aydin, A., & Johnson, N. (2015). Permeability of a fault zone crosscutting a sequence of sandstones and shales and its influence on hydraulic head distribution in the Chatsworth Formation, California, USA. *23*(2), 405-419.
- Cipolla, C., Lolon, E., Erdle, J., & Rubin, B. (2010). Reservoir Modeling in Shale-Gas Reservoirs.
- CMG. (2017). *GEM user's guide*. Calgary, Alberta, Canada: CMG Ltd.
- Croisé, J., Schlickenrieder, L., Marschall, P., Boisson, J. Y., Vogel, P., & Yamamoto, S. (2004). Hydrogeological investigations in a low permeability claystone formation: the Mont Terri Rock Laboratory. *Physics and Chemistry of the Earth, Parts A/B/C*, *29*(1), 3-15. doi:<https://doi.org/10.1016/j.pce.2003.11.008>
- Davidson, O., de Coninck, H., Loos, M., & Meyer, L. (2005). IPCC special report on carbon dioxide capture and storage. Prepared by working group III of the intergovernmental panel on climate change. In: Cambridge University Press, Cambridge, UK.
- Faulkner, D., Jackson, C., Lunn, R., Schlische, R., Shipton, Z., Wibberley, C., & Withjack, M. J. J. o. S. G. (2010). A review of recent developments concerning the structure, mechanics and fluid flow properties of fault zones. *32*(11), 1557-1575.
- Guo, Z., Li, X., & Chapman, M. (2012). A Shale Rock Physics Model and its Application in the Prediction of Brittleness Index, Mineralogy, and Porosity of the Barnett Shale.

- Huo, D., & Gong, B. (2010). *Discrete modeling and simulation on potential leakage through fractures in CO<sub>2</sub> sequestration*. Paper presented at the SPE annual technical conference and exhibition.
- IEA. (2006). *World energy outlook*: International Energy Agency.
- Ketzer, J. M., Iglesias, R. S., & Einloft, S. (2012). Reducing greenhouse gas emissions with CO<sub>2</sub> capture and geological storage. In *Handbook of climate change mitigation* (pp. 1405-1440): Springer.
- Krevor, S. C., Pini, R., Zuo, L., & Benson, S. (2012). Relative permeability and trapping of CO<sub>2</sub> and water in sandstone rocks at reservoir conditions. *48*(2).
- Land, C. (1968). Calculation of imbibition relative permeability for two-and three-phase flow from rock properties. *8*(02), 149-156.
- Liu, X., Gong, B., & Huo, D. (2010). *Numerical simulation on CO<sub>2</sub> sequestration in saline formations with natural or hydraulic fractures using a discrete modeling approach*. Paper presented at the Canadian Unconventional Resources and International Petroleum Conference.
- Loveless, S., Pluymaekers, M., Lagrou, D., De Boever, E., Doornenbal, H., & Laenen, B. (2014). Mapping the geothermal potential of fault zones in the Belgium-Netherlands border region. *59*, 351-358.
- Molina, O., Vilarrasa, V., & Zeidouni, M. (2017). Geologic Carbon Storage for Shale Gas Recovery. *Energy Procedia*, *114*, 5748-5760. doi:<https://doi.org/10.1016/j.egypro.2017.03.1713>
- Mosaheb, M., & Zeidouni, M. (2017a). *Above-zone pressure response to distinguish between fault and caprock leakage*. Paper presented at the SPE Western Regional Meeting.
- Mosaheb, M., & Zeidouni, M. (2017b). *Pressure Transient Analysis for Characterization of Lateral and Vertical Leakage through Faults*. Paper presented at the Carbon Management Technology Conference.
- Mosaheb, M., & Zeidouni, M. (2018). Above zone pressure interpretation for leaky well characterization and its identification from leaky caprock/fault. *Journal of Petroleum Science and Engineering*, *171*, 218-228.
- Nghiem, L., Shrivastava, V., Tran, D., Kohse, B., Hassam, M., & Yang, C. (2009). *Simulation of CO<sub>2</sub> storage in saline aquifers*. Paper presented at the SPE/EAGE Reservoir Characterization & Simulation Conference.
- Nicol, A., Seebeck, H., Field, B., McNamara, D., Childs, C., Craig, J., & Rolland, A. (2017). Fault permeability and CO<sub>2</sub> storage. *114*, 3229-3236.

- Padmakar, A. (2013). *Geomechanics coupled reservoir flow simulation for diagnostic fracture injection test design and interpretation in shale reservoirs*. Paper presented at the SPE Annual Technical Conference and Exhibition.
- Press, F., Siever, R., Grotzinger, J., & Jordan, T. H. (2004). *Understanding earth*: Macmillan.
- Rutqvist, J., Rinaldi, A. P., Cappa, F., Moridis, G. (2013). Modeling of fault reactivation and induced seismicity during hydraulic fracturing of shale-gas reservoirs. *107*, 31-44.
- Smith, J., Durucan, S., Korre, A., & Shi, J. (2011). Carbon dioxide storage risk assessment: Analysis of caprock fracture network connectivity. *5*(2), 226-240.
- Stangeland, A. (2007). A model for the CO<sub>2</sub> capture potential. *1*(4), 418-429.
- Starr, J. (2011). Closure stress gradient estimation of the Marcellus Shale from seismic data. In *SEG Technical Program Expanded Abstracts 2011* (pp. 1789-1793): Society of Exploration Geophysicists.
- Tran, D., Settari, A., & Nghiem, L. (2004). New iterative coupling between a reservoir simulator and a geomechanics module. *9*(03), 362-369.
- Tran, D., Shrivastava, V. K., Nghiem, L. X., & Kohse, B. F. (2009). *Geomechanical risk mitigation for CO<sub>2</sub> sequestration in saline aquifers*. Paper presented at the SPE Annual Technical Conference and Exhibition.
- Varre, S. B., Siriwardane, H. J., Gondle, R. K., Bromhal, G. S., Chandrasekar, V., & Sams, N. J. I. J. o. G. G. C. (2015). Influence of geochemical processes on the geomechanical response of the overburden due to CO<sub>2</sub> storage in saline aquifers. *42*, 138-156.
- Williams, M. (2002). Climate change: information kit. Geneva: the United Nations Environment Programme (UNEP) and the United Nations Framework Convention on Climate Change. In: UNFCCC.
- Wilson, E., & Gerard, D. (2007). Carbon capture and sequestration: integrating technology, monitoring, regulation.
- Yudhowijoyo, A., Rafati, R., Haddad, A. S., Raja, M. S., Hamidi, H. (2018). Subsurface methane leakage in unconventional shale gas reservoirs: A review of leakage pathways and current sealing techniques.
- Zhang, D., & Song, J. (2014). Mechanisms for geological carbon sequestration. *10*, 319-327.
- Zulqarnain, M., Zeidouni, M., & Hughes, R. G. (2018). Implications of fault structure heterogeneities, dissolution and capillary trapping mechanisms for CO<sub>2</sub> storage integrity. *International Journal of Greenhouse Gas Control* *76*, 53-61.

## **Vita**

Dayna Rodriguez Zambrano possesses a bachelor in Oil, Gas, and Processes Engineering (2012), and a Master of Science in Petroleum Engineering (2014) from Universidad Mayor de San Andres located in her natal city La Paz, Bolivia. During her studies, she served as a Teaching Assistant for two years. Dayna's research topics included Analytical Analysis of Gas Condensate Banking and Generation of Biogas in Landfills. After obtaining her master's degree in Bolivia, Dayna started to work as an Assistant Professor at Universidad Publica de El Alto and Centro de Formacion Profesional Brasil-Bolivia, teaching several courses including Calculus, Algebra, Drilling Engineering, Reservoir Engineering, and Production of Hydrocarbons. In 2016, Dayna was awarded a Fulbright scholarship that allowed her to study a Master of Science in Petroleum Engineering at Louisiana State University. Besides her academic chores at LSU, she was also an active member of the SPE (Society of Petroleum Engineers) and a tutor in the Chevron Mentorship Program.